ATLAS CONF Note

ATLAS-CONF-2019-019

May 24, 2019

# Search for direct production of electroweakinos in final states with missing transverse energy and a Higgs boson decaying into photons in *pp* collisions at $\sqrt{s} = 13$ TeV with the ATLAS detector

The ATLAS Collaboration

A search for a chargino-neutralino pair decaying via the 125 GeV Higgs boson into photons is presented. This study is based on the full Run 2 data collected between 2015 and 2018 with the ATLAS detector at the LHC, corresponding to an integrated luminosity of 139 $\text{fb}^{-1}$ of *pp* collisions at a centre-of-mass energy of 13 TeV. No significant excess over the expected background is observed. Upper limits at 95% confidence level for a massless $\tilde{\chi}_1^0$ are set on several electroweakino production cross sections and the visible cross section for beyond the Standard Model physics processes. In the context of simplified supersymmetric models, 95% confidence-level limits of up to 315 GeV in $m(\tilde{\chi}_1^{\pm}/\tilde{\chi}_2^0)$, where $m(\tilde{\chi}_1^0)$ is 0.5 GeV, are set. Limits at 95% confidence level are also set on the $\tilde{\chi}_1^{\pm}\tilde{\chi}_2^0$ cross section in the mass plane of $m(\tilde{\chi}_1^{\pm}/\tilde{\chi}_2^0)$ and $m(\tilde{\chi}_1^0)$.

ATLAS-CONF-2019-019
28 May 2019

# 1 Introduction

Theoretical and experimental arguments suggest that the Standard Model (SM) is an effective theory valid up to a certain energy scale. The observation by the ATLAS and CMS collaborations of a particle consistent with the SM Higgs boson [1–4], referred to as $h$, has brought renewed attention to the mechanism of electroweak symmetry breaking and the hierarchy problem [5–8]: the Higgs boson mass is strongly sensitive to quantum corrections from physics at very high energy scales and demands a high level of fine-tuning. Supersymmetry (SUSY) [9–14] resolves the hierarchy problem by introducing for each known boson or fermion a new partner (superpartner) that shares the same mass and internal quantum numbers if supersymmetry is unbroken. However, these superpartners have not been observed, so SUSY must be a broken symmetry and the mass scale of the supersymmetric particles is as yet undetermined. The possibility of a supersymmetric dark matter (DM) candidate [15, 16] is related closely to the conservation of $R$-parity [17]. Under the $R$-parity conservation hypothesis, the lightest supersymmetric particle (LSP) is stable. If the LSP is weakly interacting, it may provide a viable DM candidate. The nature of the LSP is defined by the mechanism that spontaneously breaks supersymmetry and the parameters of the chosen theoretical framework.

In the SUSY scenarios considered as benchmarks in this paper, the LSP is the lightest of the neutralinos ($\tilde{\chi}^0$) which, together with the charginos ($\tilde{\chi}^\pm$), represent the mass eigenstates formed from the mixture of the $\gamma$, $W$, $Z$ and Higgs bosons' superpartners (the Higgsinos, winos and binos). The neutralinos and charginos are collectively referred to as *electroweakinos*. Specifically, the electroweakino mass eigenstates are designated in order of increasing mass as $\tilde{\chi}^\pm_i$ $(i = 1, 2)$ (charginos) and $\tilde{\chi}^0_j$ $(j = 1, 2, 3, 4)$ (neutralinos). In the primary model considered in this paper, the compositions of the lightest chargino ($\tilde{\chi}^\pm_1$) and next-to-lightest neutralino ($\tilde{\chi}^0_2$) are wino-like and the two particles are nearly mass degenerate, while the lightest neutralino ($\tilde{\chi}^0_1$) is assumed to be bino-like. The results are also interpreted in the context of a model inspired by Gauge-Mediated Supersymmetry Breaking (GMSB) [18–20], for which the LSP is the gravitino $\tilde{G}$ (the superpartner of a graviton, the hypothesized quantum of the gravitational field), with the lightest electroweakinos being the nearly-degenerate set of the four Higgsino states.

Naturalness considerations [21, 22] suggest that the lightest of the charginos and neutralinos have masses near the electroweak scale. Their direct production may be the dominant mechanism at the Large Hadron Collider (LHC) if the superpartners of the gluon and quarks are heavier than a few TeV. In SUSY models where the masses of the heaviest (pseudoscalar, charged) Minimal Supersymmetric Standard Model (MSSM) Higgs bosons and the superpartners of the leptons have masses larger than those of the lightest chargino and next-to-lightest neutralino, the former might decay into the $\tilde{\chi}^0_1$ and a $W$ boson ($\tilde{\chi}^\pm_1 \rightarrow W\tilde{\chi}^0_1$), while the latter could decay into the $\tilde{\chi}^0_1$ and the lightest MSSM Higgs boson or $Z$ boson ($\tilde{\chi}^0_2 \rightarrow h/Z\tilde{\chi}^0_1$) [17, 23, 24]. The decay via the Higgs boson is dominant for many choices of the parameters as long as the mass-splitting between the two lightest neutralinos is larger than the Higgs boson mass and the Higgsinos are heavier than the winos. SUSY models of this kind, where sleptons are heavier than $\tilde{\chi}^\pm_1$ and $\tilde{\chi}^0_2$ but not too heavy, could provide a possible explanation for the discrepancy between measurements of the muon's anomalous magnetic moment $g - 2$ and SM predictions [25–28].

This paper presents a search in $pp$ collisions produced at the LHC at a centre-of-mass energy $\sqrt{s} = 13$ TeV for the direct pair production of electroweakinos that promptly decay into the LSP, producing at least one SM-like Higgs boson decaying to two photons in each event. Although there is a small branching fraction of the Higgs boson decaying into a pair of photons, the diphoton system gives a narrow mass peak around the Higgs boson mass. By using the highly efficient diphoton trigger, the channel presented in this paper provides more sensitivity in the low missing transverse energy ($E_{\mathrm{T}}^{\mathrm{miss}}$) region and therefore is complementary to other channels [29]. The primary model, for which the search is optimized, involves the production of a chargino in association with a next-to-lightest neutralino, which promptly decay as $\tilde{\chi}_1^\pm \to W\tilde{\chi}_1^0$ and $\tilde{\chi}_2^0 \to h\tilde{\chi}_1^0$ respectively (see Figure 1 (a)). A simplified SUSY model [30, 31] is considered for the optimization of the search and the interpretation of results. The $\tilde{\chi}_1^\pm \to W\tilde{\chi}_1^0$ and $\tilde{\chi}_2^0 \to h\tilde{\chi}_1^0$ decays are each assumed to have a 100% branching fraction. The Higgs boson branching fractions are assumed to be the same as in the SM. New to this search, this paper makes use of the inclusive decays of the $W$ boson. In addition, a prior search [29] from ATLAS for this model making use of 36.1 fb$^{-1}$ $pp$ collision data, based purely on leptonic decays of the $W$ boson, observed a mild excess of events above the SM prediction. An identical "follow-up" analysis, updated for the full Run 2 data, is presented here as well.

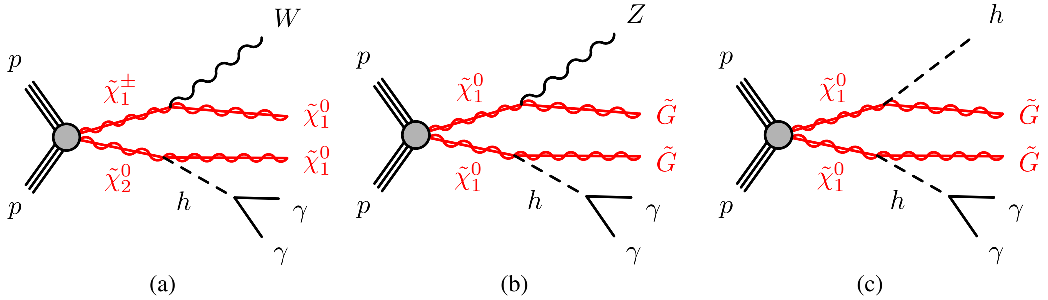

Figure 1: The signal diagrams illustrating (a) $\tilde{\chi}_1^\pm\tilde{\chi}_2^0$ production, and two Higgsino production modes from a GMSB model: (b) $\tilde{\chi}_1^0 \to Z\tilde{G}$ and $\tilde{\chi}_1^0 \to h\tilde{G}$, (c) $\tilde{\chi}_1^0 \to h\tilde{G}$. For $\tilde{\chi}_1^\pm\tilde{\chi}_2^0$ production, the lightest chargino ($\tilde{\chi}_1^\pm$) and next-to-lightest neutralino ($\tilde{\chi}_2^0$) are nearly mass degenerate. In the Higgsino models, the two lightest neutralinos ($\tilde{\chi}_1^0, \tilde{\chi}_2^0$), and the lightest chargino ($\tilde{\chi}_1^\pm$) are approximately mass degenerate, and the $\tilde{\chi}_1^0$ is the lightest of the four nearly-degenerate Higgsino states.

The analysis optimized for the search for $\tilde{\chi}_1^\pm\,\tilde{\chi}_2^0$ production is also used to search for two closely-related GMSB scenarios featuring direct production of pairs of Higgsinos [32–34], collectively referred to as $\tilde{\chi}\tilde{\chi}$. In this model, the two lightest neutralinos $\tilde{\chi}_1^0$, $\tilde{\chi}_2^0$, and the lightest chargino $\tilde{\chi}_1^\pm$ are approximately mass degenerate, and the $\tilde{\chi}_1^0$ is the lightest of the four nearly-degenerate Higgsino states. It is assumed that $m(\tilde{\chi}_1^\pm) = m(\tilde{\chi}_2^0) = m(\tilde{\chi}_1^0) + 1$ GeV in this model. The Higgsino $\tilde{\chi}_2^0$ and $\tilde{\chi}_1^\pm$ can decay into a $\tilde{\chi}_1^0$ and SM particles with low transverse momentum. The Higgsino $\tilde{\chi}_1^0$, as the next-to-lightest SUSY particle (NLSP), will decay to a gravitino $\tilde{G}$ and a $h$/Z boson, where the LSP $\tilde{G}$ is the SUSY partner of the graviton. The effective cross section for the Higgsino production is a combination of the cross sections of $\tilde{\chi}_1^0\,\tilde{\chi}_2^0$, $\tilde{\chi}_1^0\,\tilde{\chi}_1^\pm$, $\tilde{\chi}_2^0\,\tilde{\chi}_1^\pm$, and $\tilde{\chi}_1^\pm\,\tilde{\chi}_1^\mp$ production. In the first of GMSB scenarios considered in this paper (Figure 1 (b)), a 50% branching fraction of $\tilde{\chi}_1^0 \to h\tilde{G}$ and $\tilde{\chi}_1^0 \to Z\tilde{G}$ is assumed. This scenario will be referred to as $h\tilde{G}Z\tilde{G}$ in the following. In the second scenario (Figure 1 (c)), $h\tilde{G}h\tilde{G}$ in the following, a 100% branching fraction of $\tilde{\chi}_1^0 \to h\tilde{G}$ is assumed. In both scenarios, each $\tilde{G}$ in the final state is nearly massless, stable, and weakly interacting which leads to a $E_{\mathrm{T}}^{\mathrm{miss}}$ signature.

This paper is organized as follows. Section 2 presents a brief description of the ATLAS detector. Section 3 introduces the data and the signal and background Monte Carlo (MC) simulation samples used. Section 4 outlines the event reconstruction, while Section 5 explains the optimization of the event selection and categorization. Section 6 discusses the signal and background modeling. Section 7 summarizes the experimental and theoretical systematic uncertainties that affect the results. Section 8 describes the results and their interpretations, and a summary of the results is given in Section 9.

## 2 ATLAS detector

The ATLAS detector [35] is a multipurpose particle detector with a forward–backward symmetric cylindrical geometry and nearly $4\pi$ coverage in solid angle.[1] The inner tracking detector (ID) consists of pixel and microstrip silicon detectors covering the pseudorapidity region $|\eta| < 2.5$, surrounded by a transition radiation tracker which enhances electron identification in the region $|\eta| < 2.0$. A new inner pixel layer, the insertable B-layer [36, 37], was added at a mean radius of 3.3 cm during the period between Run 1 and Run 2 of the LHC. The inner detector is surrounded by a thin superconducting solenoid providing an axial 2 T magnetic field and by a fine-granularity lead/liquid-argon (LAr) electromagnetic (EM) sampling calorimeter covering $|\eta| < 3.2$. A steel/scintillator-tile hadronic sampling calorimeter provides coverage in the central pseudorapidity range ($|\eta| < 1.7$). The endcap and forward regions ($1.5 < |\eta| < 4.9$) of the hadronic calorimeter are made of LAr active layers with either copper or tungsten as the absorber material. A muon spectrometer with an air-core toroid magnet system surrounds the calorimeters. Three layers of high-precision tracking chambers provide coverage in the range $|\eta| < 2.7$, while dedicated fast chambers allow triggering in the region $|\eta| < 2.4$. The ATLAS trigger system consists of a hardware-based level-1 trigger followed by a software-based high-level trigger [38].

## 3 Data and simulation samples

The analysis uses $pp$ collision data with a bunch crossing interval of 25 ns, collected from 2015 to 2018 at $\sqrt{s} = 13$ TeV. Events that were recorded in stable beam conditions, when relevant detector components were functioning properly, are considered. A diphoton trigger is used to collect the events by requiring two reconstructed photon candidates with transverse energies ($E_{\mathrm{T}}$) of at least 35 GeV and 25 GeV for the $E_{\mathrm{T}}$-ordered leading and subleading photons respectively. The trigger efficiency with respect to the offline-reconstructed photons, measured using the same method as described in Ref. [39], is 99%. The data sample corresponds to an integrated luminosity of $139.0 \pm 2.4\ \mathrm{fb}^{-1}$. There are on average 25 to 38 interactions in the same bunch crossing (in-time pileup) in this data sample.

The MC simulation of signal and background processes is used to optimize the selection criteria, estimate uncertainties and study the shapes of the signal and background diphoton invariant mass ($m_{\gamma\gamma}$) distributions. Signal events are generated with up to two additional partons in the matrix element using MadGraph_aMC@NLO 2.6.2 [40] at leading order (LO) in quantum chromodynamics (QCD) using the NNPDF3.0LO [41] parton distribution function (PDF) set and CKKW-L merging scheme. Parton showering and hadronization are handled by the Pythia 8.230 [42] event generator with the A14 [43] set of tuned parameters (tune), using the NNPDF2.3LO PDF set [44]. MC samples for the $\tilde{\chi}_1^{\pm}\tilde{\chi}_2^0$ production are generated assuming a 0.5 GeV $\tilde{\chi}_1^0$ mass. As shown in Figure 2 (a), with a higher value of $m(\tilde{\chi}_1^{\pm}/\tilde{\chi}_2^0)$, the $p_{\mathrm{T}}$ distribution of the $\tilde{\chi}_1^0\tilde{\chi}_1^0$ system is broader. The $p_{\mathrm{T}}$ distributions of $\tilde{G}\tilde{G}$ system for the Higgsino production of $h\tilde{G}h\tilde{G}$, $h\tilde{G}Z\tilde{G}$ are presented in Figure 2 (b) and (c). The MC samples include $\tilde{\chi}_1^0\,\tilde{\chi}_2^0$, $\tilde{\chi}_1^0\,\tilde{\chi}_1^{\pm}$, $\tilde{\chi}_2^0\,\tilde{\chi}_1^{\pm}$, and $\tilde{\chi}_1^{\pm}\,\tilde{\chi}_1^{\mp}$ production. The kinematic distributions strongly depend on the mass of $\tilde{\chi}_1^0$, where the mass of the $\tilde{G}$ is assumed to be 1 MeV.

---

[1] ATLAS uses a right-handed coordinate system with its origin at the nominal interaction point in the centre of the detector. The positive $x$-axis is defined by the direction from the interaction point to the centre of the LHC ring, with the positive $y$-axis pointing upwards, while the beam direction defines the $z$-axis. Cylindrical coordinates $(r, \phi)$ are used in the transverse plane, $\phi$ being the azimuthal angle around the $z$-axis. The pseudorapidity $\eta$ is defined in terms of the polar angle $\theta$ by $\eta = -\ln\tan(\theta/2)$. Rapidity is defined as $y = 0.5\ln[(E + p_z)/(E - p_z)]$ where $E$ denotes the energy and $p_z$ is the component of the momentum along the beam direction. The angular distance $\Delta R$ is defined as $\sqrt{(\Delta y)^2 + (\Delta\phi)^2}$.

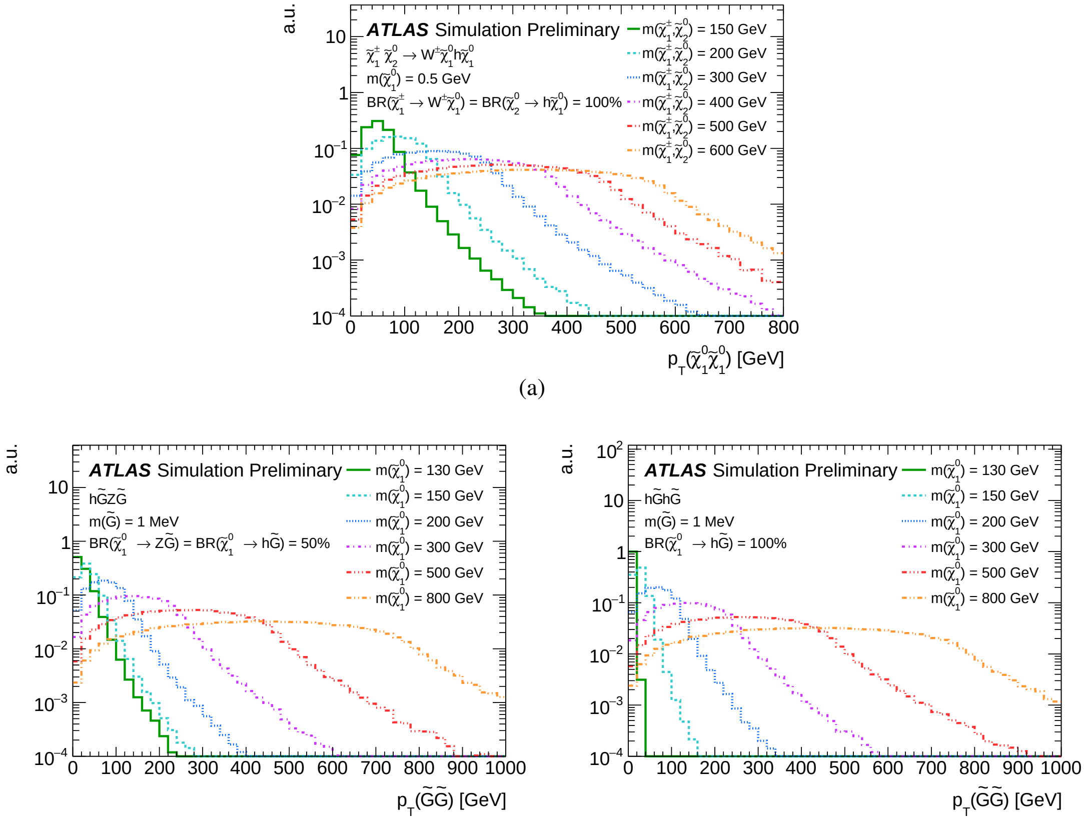

(a)

(b)

(c)

Figure 2: The $p_{\mathrm{T}}$ distribution of $\tilde{\chi}_1^0\tilde{\chi}_1^0$ and $\tilde{G}\tilde{G}$ system in (a) $W^{\pm}\tilde{\chi}_1^0 h\tilde{\chi}_1^0$, (b) $h\tilde{G}Z\tilde{G}$, and (c) $h\tilde{G}h\tilde{G}$ production.

The dominant backgrounds are resonant SM $h \rightarrow \gamma\gamma$ processes, and non-resonant processes which include $\gamma\gamma$, $\gamma$+jet, $W\gamma$, $Z\gamma$, $W\gamma\gamma$ and $Z\gamma\gamma$ production. For the production of resonant SM Higgs bosons, events from the $Wh$ and $Zh$ processes are generated with Pythia 8.186 with the A14 tune and the NNPDF2.3LO PDF set. The gluon-fusion (ggF) and vector-boson fusion (VBF) samples are generated with Powheg-Box v2 [45–48] interfaced to Pythia 8.186 with the AZNLO [49] tune and the CT10 PDF set [50]. Samples of $t\bar{t}h$ events are generated with MadGraph_aMC@NLO 2.2.3 [40] interfaced to Pythia 8.186 with the NNPDF3.0LO [41] PDF set. Samples of $b\bar{b}h$ events are generated with MadGraph_aMC@NLO 2.2.3 interfaced to Pythia 8.186 with the A14 tune and the NNPDF2.3LO PDF set. The non-resonant diphoton processes with associated jets are generated using Sherpa 2.2.4 [51]. Matrix elements are calculated with up to three partons at LO and merged with the Sherpa 2.2.4 parton shower [52] using the ME+PS@LO prescription [53]. The CT10 PDF set is used in conjunction with a dedicated parton-shower tuning developed by the authors of Sherpa 2.2.4. The $W\gamma$, $Z\gamma$, $W\gamma\gamma$, $Z\gamma\gamma$ samples are generated using Sherpa 2.2.4 with the CT10 PDF set.

Both the shape and normalization of the total non-resonant background are obtained directly from data, as described in Section 6. The cross sections [54] of the SM Higgs-boson processes are calculated at next-to-leading order (NLO) in electroweak theory and next-to-next-to-leading order (NNLO) in QCD for VBF, $Zh$ and $Wh$ samples and next-to-next-to-next-to-leading order plus next-to-next-to-leading logarithm (N$^3$LO+NNLL) in QCD for the ggF sample. The SM Higgs-boson mass is set to 125.09 GeV [3] and its branching fraction decaying into two photons is 0.227% [54]. Signal cross sections are calculated to next-to-leading order in the strong coupling constant, adding the resummation of soft gluon emission at next-to-leading-logarithmic accuracy (NLO+NLL) [55–58]. The nominal cross section and the uncertainty are taken from an envelope of cross section predictions using different PDF sets and factorisation and renormalisation scales, as described in Ref. [59].

Different pileup conditions from same and neighboring bunch crossings as a function of the instantaneous luminosity are simulated by overlaying minimum-bias events generated with Pythia 8.186 and EvtGen [60] with the MSTW2008LO PDF set and the A3 [61] tune on the events of all hard processes. Differences between the simulated and observed distributions of the number of interactions per bunch crossing are corrected by applying weights to simulated events. Detector effects are simulated using a full simulation [62] performed using Geant4 [63] for signals, SM Higgs processes, and $W\gamma$, $Z\gamma$, $W\gamma\gamma$ and $Z\gamma\gamma$ backgrounds. The diphoton continuum background and some of the signal samples are simulated using a fast simulation of the calorimeter based on AtlFastII [62].

## 4 Event reconstruction

Photons are reconstructed in the region $|\eta| < 2.37$ excluding $1.37 < |\eta| < 1.52$ from clusters of energy deposits in the EM calorimeters. Clusters without a matching track or reconstructed conversion vertex in the inner detector are classified as unconverted photons. Those with a matching reconstructed conversion vertex or with a matching track, consistent with originating from a photon conversion, are classified as converted photons. The other ones are classified as electrons. The photon energy is calibrated using a multivariate regression algorithm trained with fully reconstructed MC samples and then corrected based on data-driven techniques on data [64]. The overall energy scale in data, as well as the data-to-MC difference in the constant term of the energy resolution, are estimated from a sample of $Z$ boson decays to electrons recorded in 2015 and 2016 [65]. The photon direction is estimated either using EM calorimeter longitudinal segmentation (if unconverted) or conversion vertex position (if converted), together with constraints from the $pp$ collision point.

In order to reduce the misidentification of hadronic jets containing a high-$p_{\mathrm{T}}$ neutral hadron (e.g. $\pi^0$) decaying to two photons, a “Tight” identification criteria [66] is applied. The photon identification is based on the lateral profile of the energy deposits in the first and second layers of the EM calorimeter, and on the shower leakage fraction in the hadronic calorimeter. The selection requirements are tuned for converted and unconverted photon candidates separately. The identification efficiency of unconverted (converted) photons ranges from 85% to 95% (90% to 98%) between 25 GeV and 200 GeV [67]. Corrections are applied to the EM shower-shape variables for simulated photons, to account for small differences between data and simulation.

To further suppress hadronic backgrounds, requirements on two photon isolation variables are applied. The first variable, $E_{\mathrm{T}}^{\mathrm{iso}}$, calculates the sum of the transverse energies deposited in topological clusters [68] of cells in the calorimeter within a cone of size $\Delta R = 0.2$ around each photon. The photon cluster energy and an estimate of the energy deposited by the photon outside its associated cluster is also subtracted from this sum. To reduce the underlying event and pileup effects, $E_{\mathrm{T}}^{\mathrm{iso}}$ is further corrected using the method described in Refs. [69, 70]. The second variable is a track-based isolation, defined as the scalar sum of the transverse momenta of all tracks with $p_{\mathrm{T}} > 1$ GeV and consistent with originating from the primary vertex (PV) within a cone of size $\Delta R = 0.2$ around each photon. The isolation efficiency for photons, which is mostly independent of their kinematic variables, is about 90% for the gluon-gluon fusion SM Higgs boson process.

Events are required to have at least one PV, defined as the vertex associated with at least two tracks with $p_{\text{T}} > 0.5$ GeV and with the highest sum of squared transverse momenta of associated tracks [71]. In each event, PV most likely to be the origin of the diphoton, selected from the PV candidates using a neural network, is required to be consistent with the event PV. The input variables to this neural network are the combined $z$-position of the intersections of the extrapolated photon trajectories with the beam axis; the sum of the squared transverse momenta $\sum p_{\text{T}}^2$ and the scalar sum of the transverse momenta $\sum p_{\text{T}}$ of the tracks associated with each reconstructed vertex; and the difference in azimuthal angle $\Delta\phi$ between the direction defined by the vector sum of the momenta of tracks from each vertex and that of the diphoton system. Dedicated studies of $Z \to e^+e^-$ events are performed in order to validate the diphoton vertex identification efficiency (correct identification of the hard process vertex by the neural network) between data and simulation. The method is similar to the one used in Ref. [72].

Electrons are reconstructed from energy deposits measured in the EM calorimeter which are matched to ID tracks [73]. They are required to satisfy $|\eta| < 2.47$, excluding the EM calorimeter transition region $1.37 < |\eta| < 1.52$, and to have $p_{\text{T}} > 10$ GeV. The electrons are identified using a likelihood-based algorithm that uses the track and shower-shape variables. The "MediumLLH" criteria are applied, providing a good identification efficiency varying from 85% to 95% as a function of $E_{\text{T}}$ [74]. Loose calorimeter and track isolation requirements are applied to electrons. The efficiency of the isolation requirements is 98% [75].

Muons are reconstructed from high-quality track segments in the muon spectrometer. In the region $|\eta| < 2.5$, they must be matched to ID tracks. They are required to have $p_{\text{T}} > 10$ GeV and $|\eta| < 2.7$ [76]. The muon "medium" criteria are applied with a 96% [77] identification efficiency. The muon candidates must also satisfy calorimeter and track isolation criteria. The combined isolation efficiency varies from 95% to 99% as a function of $p_{\text{T}}$ from 25 GeV to 60 GeV [77].

The significance of the track's transverse impact parameter with respect to the PV, $|d_0|/\sigma_{d_0}$, is required to be less than 5.0 for electrons and 3.0 for muons. The longitudinal impact parameter $z_0$ must satisfy $|z_0| \sin\theta < 0.5$ mm for electrons and muons.

Jets are reconstructed from three-dimensional topological clusters using the anti-$k_t$ algorithm [78] with a radius parameter of $R = 0.4$. The jets are required to have $p_{\text{T}} > 20$ GeV and $|\eta| < 4.5$ for the $E_{\text{T}}^{\text{miss}}$ calculation and $p_{\text{T}} > 25$ GeV and $|\eta| < 4.4$ for the event selection. The jets with $|\eta| < 2.4$ and $p_{\text{T}} < 60$ GeV must pass the jet vertex tagger (JVT) selection [79], in which a jet is identified as originating from the PV by examining the likelihood value calculated from the track information. In addition, quality criteria are applied to the jets, and events with jets consistent with noise in the calorimeter or non-collision backgrounds are vetoed [80].

Reconstruction ambiguities between photons, leptons, and jets are resolved with an "overlap removal" procedure among all the objects in the following order. First, electrons, muons, and jets found within $\Delta R = 0.4$ of a photon are removed. Next, jets found within $\Delta R = 0.2$ of an electron are removed. Electrons and muons within $\Delta R = 0.4$ of the remaining jets are removed last. A different overlap removal strategy was used in the previous study [29] and the selection discussed in Section 5.2. It was motivated by the prioritization of electrons, as opposed to photons. The results show no significant difference in sensitivity between these two strategies.

Jets containing a $b$-hadron are identified using the MV2c10 [81, 82] multivariate discriminant built with information from track impact parameters and the presence of reconstructed secondary vertices, which applies a multi-vertex fitter to reconstruct the hadron decay chain of $b \to c$. A working point is chosen that provides a $b$-tagging efficiency of 70% in simulated $t\bar{t}$ events. The misidentification rates for $c$-jets and jets originating from gluons or light ($u$, $d$, $s$) quarks are 8.2% and 0.3%, respectively. An additional energy correction is applied to $b$-jets to account for the presence of muons in the jet [83].

The $E_{\mathrm{T}}^{\mathrm{miss}}$ is calculated as the negative vectorial sum of the transverse momenta of calibrated photons, electrons, muons and jets associated with the PV. The transverse momenta of all tracks that originate from the PV but are not already used in the $E_{\mathrm{T}}^{\mathrm{miss}}$ calculation are summed and taken into account in the $E_{\mathrm{T}}^{\mathrm{miss}}$ calculation. This term is defined as the track-based soft term [84, 85]. Clusters and tracks not associated with the PV are not included in the $E_{\mathrm{T}}^{\mathrm{miss}}$ calculation, significantly suppressing the effect of pileup and thus improving the $E_{\mathrm{T}}^{\mathrm{miss}}$ resolution.

# 5 Event selection

## 5.1 Baseline selection

Each event is required to contain at least two photons with $p_{\mathrm{T}} > 22$ GeV and within the fiducial region in the EM calorimeters defined as $|\eta| < 2.37$, excluding the region $1.37 < |\eta| < 1.52$. The photons are ordered by their $p_{\mathrm{T}}$. The leading and subleading photons are required to have $p_{\mathrm{T}}^{\gamma}/m_{\gamma\gamma} > 0.35$ and 0.25, respectively, where $m_{\gamma\gamma}$ is the invariant mass of the leading and subleading photon pair. The signal region is defined as 105 GeV $< m_{\gamma\gamma} <$ 160 GeV where $m_{\gamma\gamma}$ is calculated using photon 4-vectors recomputed with respect to the PV. The PV is required to have the largest $\Sigma p_{\mathrm{T}}^2$, where $p_{\mathrm{T}}$ is the transverse momentum of the tracks associated with the vertex. The selected events are divided into twelve categories based on the number of leptons ($N_\ell$), number of jets ($N_j$), the invariant mass of the two highest $p_{\mathrm{T}}$ jets ($M_{jj}$), and the $E_{\mathrm{T}}^{\mathrm{miss}}$ significance $S_{E_{\mathrm{T}}^{\mathrm{miss}}} = E_{\mathrm{T}}^{\mathrm{miss}}/\sqrt{\sum E_{\mathrm{T}}}$, in which the total transverse energy $\sum E_{\mathrm{T}}$ is calculated from the scalar sum of the transverse momenta of the calibrated photons, electrons, muons and jets used in the $E_{\mathrm{T}}^{\mathrm{miss}}$ calculation described in Section 4, as well as the tracks not associated with these but associated to the PV. No $b$-jet veto is applied in the baseline selection. The twelve categories are defined in Table 1. The sample of $\tilde{\chi}_1^{\pm}\,\tilde{\chi}_2^0$ signal with $m(\tilde{\chi}_1^{\pm}/\tilde{\chi}_2^0) = 150$ GeV and $m(\tilde{\chi}_1^0) = 0.5$ GeV is used to optimize the boundary of each category to maximize the significance combining all the twelve categories. The Leptonic and Hadronic categories are used to accommodate the most clearly identifiable leptonic and hadronic decays of the $W$ boson, while the Rest category retains all additional signal-like topologies. In each region the events are sliced into $S_{E_{\mathrm{T}}^{\mathrm{miss}}}$ bins to improve the sensitivity because different signal models have different $p_{\mathrm{T}}$ distributions of the $\tilde{\chi}_1^0\tilde{\chi}_1^0$ system as shown in Figure 2. The signal $\tilde{\chi}_1^{\pm}\tilde{\chi}_2^0 \to \tilde{\chi}_1^0 W^{\pm}\tilde{\chi}_1^0 h$ has the highest expected significance in the Leptonic categories, and the $h\tilde{G}Z\tilde{G}$, $h\tilde{G}h\tilde{G}$ signals get the highest expected significance in the Rest categories.

Figure 3 shows the distribution of $S_{E_{\mathrm{T}}^{\mathrm{miss}}}$ after the selection of diphoton candidates in 120 GeV $< m_{\gamma\gamma} <$ 130 GeV. Expected distributions are shown for the $\tilde{\chi}_1^{\pm}\tilde{\chi}_2^0 \to W^{\pm}\tilde{\chi}_1^0 h\tilde{\chi}_1^0$ signal with $m(\tilde{\chi}_1^{\pm}/\tilde{\chi}_2^0) = 200$ GeV, $m(\tilde{\chi}_1^0) = 0.5$ GeV, and $h\tilde{G}Z\tilde{G}$, $h\tilde{G}h\tilde{G}$ signal with $m(\tilde{\chi}_1^0) = 150$ GeV, $m(\tilde{G}) = 1$ MeV. These overlaid signal points are representative of the model kinematics. The shapes and normalizations of the $V\gamma$ and $V\gamma\gamma$ contributions are obtained from the MC simulation. The shape of the $\gamma\gamma$ contribution is obtained from the MC simulation while the normalization is fixed to the yields of the data sideband multiplied by the diphoton purity among all the backgrounds. The diphoton purity is measured in the data, using a two-dimensional sideband technique by counting the number of events in which one or both photons pass or fail the identification or isolation requirements [86]. The diphoton purity varies from 65% to 93% for different categories. The shape of the $\gamma$+jet contribution is obtained using the data distribution in a

Table 1: Criteria used in the categorization.

| Channels | Names | Selection |
|---|---|---|
| Leptonic | Category 1 | $0 < S_{E_T^{\text{miss}}} \leq 2,\, N_\ell \geq 1$ |
| | Category 2 | $2 < S_{E_T^{\text{miss}}} \leq 4,\, N_\ell \geq 1$ |
| | Category 3 | $4 < S_{E_T^{\text{miss}}} \leq 6,\, N_\ell \geq 1$ |
| | Category 4 | $S_{E_T^{\text{miss}}} > 6,\, N_\ell \geq 1$ |
| Hadronic | Category 5 | $5 < S_{E_T^{\text{miss}}} \leq 6,\, N_\ell = 0,\, N_j \geq 2,\, M_{jj} \in [40, 120]$ GeV |
| | Category 6 | $6 < S_{E_T^{\text{miss}}} \leq 7,\, N_\ell = 0,\, N_j \geq 2,\, M_{jj} \in [40, 120]$ GeV |
| | Category 7 | $7 < S_{E_T^{\text{miss}}} \leq 8,\, N_\ell = 0,\, N_j \geq 2,\, M_{jj} \in [40, 120]$ GeV |
| | Category 8 | $S_{E_T^{\text{miss}}} > 8,\, N_\ell = 0,\, N_j \geq 2,\, M_{jj} \in [40, 120]$ GeV |
| Rest | Category 9 | $6 < S_{E_T^{\text{miss}}} \leq 7,\, N_\ell = 0,\, N_j < 2$ or ( $N_j \geq 2,\, M_{jj} \notin [40, 120]$ GeV) |
| | Category 10 | $7 < S_{E_T^{\text{miss}}} \leq 8,\, N_\ell = 0,\, N_j < 2$ or ( $N_j \geq 2,\, M_{jj} \notin [40, 120]$ GeV) |
| | Category 11 | $8 < S_{E_T^{\text{miss}}} \leq 9,\, N_\ell = 0,\, N_j < 2$ or ( $N_j \geq 2,\, M_{jj} \notin [40, 120]$ GeV) |
| | Category 12 | $S_{E_T^{\text{miss}}} > 9,\, N_\ell = 0,\, N_j < 2$ or ( $N_j \geq 2,\, M_{jj} \notin [40, 120]$ GeV) |

control region where the event selection is the same as the signal region but one of the photons fails the identification criteria, after subtracting the contamination from $\gamma\gamma$, $V\gamma$ and $V\gamma\gamma$ using MC simulation. Its normalization is fixed to the $\gamma$+jet purity varying from 34% to 7% for different categories.

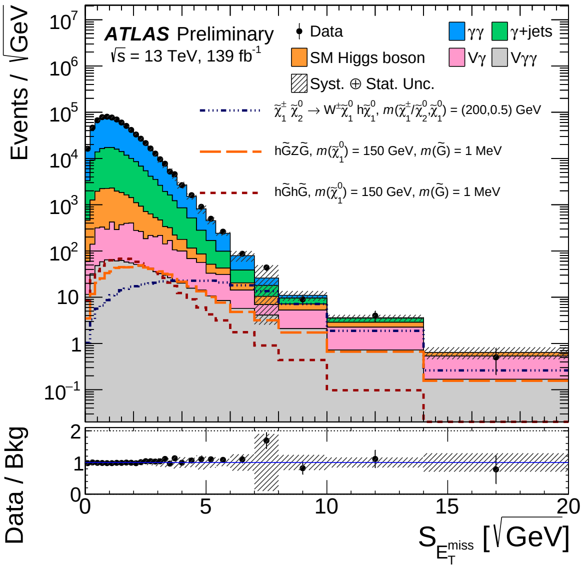

Figure 3: The distribution of $S_{E_T^{\text{miss}}}$ after the selection of diphoton candidates in 120 GeV $< m_{\gamma\gamma} <$ 130 GeV. Expected distributions are shown for the $\tilde{\chi}_1^\pm\tilde{\chi}_2^0 \to W^\pm\tilde{\chi}_1^0 h\tilde{\chi}_1^0$ signal with $m(\tilde{\chi}_1^\pm/\tilde{\chi}_2^0)$ = 200 GeV, $m(\tilde{\chi}_1^0)$ = 0.5 GeV, and $h\tilde{G}Z\tilde{G}$, $h\tilde{G}h\tilde{G}$ signal with $m(\tilde{\chi}_1^0)$ = 150 GeV, $m(\tilde{G})$ = 1 MeV. These overlaid signal points are representative of the model kinematics. Only the quadratic sum of the MC statistical and experimental systematic uncertainties in the total background is shown as the hatched bands, while the theoretical uncertainties in the background normalization are not included. Overflow events are included in the rightmost bin.

### 5.2 Excess follow-up selection

In order to check the mild excess of events observed in the previous search [29] from ATLAS using 36.1 fb$^{-1}$ $pp$ collision data, two signal regions ('SR1L$\gamma\gamma$-a' and 'SR1L$\gamma\gamma$-b') defined in the previous search are reused in this analysis. Events are required to have exactly one lepton with $p_{\mathrm{T}} > 25$ GeV and exactly two photons with $p_{\mathrm{T}}$ >40 (30) GeV for the leading (sub-leading) photon. The invariant mass of the two photons is required to be 105 GeV $< m_{\gamma\gamma} <$ 160 GeV, and the $E_{\mathrm{T}}^{\mathrm{miss}}$ is required to be greater than 40 GeV. The azimuthal angular difference in the transverse plane between the diphoton system and the lepton plus $E_{\mathrm{T}}^{\mathrm{miss}}$ vector is required to be greater than 2.25. In order to reduce contributions from $ttH$, a $b$-jet veto is used in all the signal regions.

To further reduce the contributions from SM backgrounds, the transverse mass $M_{\mathrm{T}}^{\mathrm{W}}$ [29] of the lepton and $E_{\mathrm{T}}^{\mathrm{miss}}$, and the three-body transverse mass $M_{\mathrm{T}}^{\mathrm{W}\gamma i}$ [29] of the lepton, $E_{\mathrm{T}}^{\mathrm{miss}}$ and the $i^{th}$ photon are used to define the two orthogonal signal regions. Common to both signal regions, events are required to have $M_{\mathrm{T}}^{\mathrm{W}\gamma 1} > 150$ GeV and $M_{\mathrm{T}}^{\mathrm{W}\gamma 2} > 80$ GeV. The first signal region, 'SR1L$\gamma\gamma$-a', is defined by $M_{\mathrm{T}}^{\mathrm{W}} > 110$ GeV and $M_{\mathrm{T}}^{\mathrm{W}\gamma 2} > 140$ GeV. Events failing these final cuts fall into the second signal region ('SR1L$\gamma\gamma$-b').

## 6 Signal and background parameterization

The signals and the SM Higgs-boson background are described independently using double-sided Crystal Ball functions (as defined in Ref. [87]). The parameters of the functions are extracted by fitting the diphoton invariant mass distributions of the MC simulation for each category. The expected normalizations are calculated from the theoretical cross sections multiplied by the acceptance and efficiency from the MC simulation.

The normalization and shape of the non-resonant background are extracted by fitting the diphoton invariant mass distribution in data for each category. Several candidate analytic functions are chosen for the non-resonant background parameterization: the exponential functions of different-order polynomials, Bernstein polynomials of different order, and an adapted dijet function [88]. The potential bias of each functional form modeling the continuum background is estimated for each category, noted as $\Delta N_{\mathrm{bkg}}^{\mathrm{non-res}}$. It is defined as the maximal signal yield extracted from the fit to a continuum-background-only diphoton invariant mass distribution, which is taken from MC simulations and is normalized to the luminosity of 139 fb$^{-1}$, with small statistical uncertainty using a signal-plus-background model, while varying the Higgs peak position from 115 GeV to 135 GeV [89]. This is to ensure the bias from choosing different background models is conservatively estimated. The functional form with the $\Delta N_{\mathrm{bkg}}^{\mathrm{non-res}}$ lower than 20% of the statistical uncertainty in data and with the fewest free parameters is chosen as the nominal background function. The $\Delta N_{\mathrm{bkg}}^{\mathrm{non-res}}$ value of the chosen functional form is taken as the non-resonant background modeling uncertainty in each category and is shown in Table 2.

## 7 Systematic uncertainties

Uncertainties from experimental and theoretical sources that affect the signal efficiency and the SM Higgs-boson background yield are estimated from the MC simultation. The non-resonant background is obtained directly from the fit to the data. The only systematic uncertainty in the non-resonant background is the

Table 2: The analytic functions to model the non-resonant background, the extracted signals from the background-only fits ($\Delta N_{\mathrm{bkg}}^{\mathrm{non-res}}$) and the relative uncertainty in the non-resonant background ($\Delta N_{\mathrm{bkg}}^{\mathrm{non-res}}/N_{\mathrm{bkg}}^{\mathrm{non-res.}}$) for each category. The variable $x$ is defined as $m_{\gamma\gamma}/\sqrt{s}$ while $a$ and $b$ are parameters of the background functions. $C_3^j$ are binomial coefficients and $b_{j,3}$ are Bernstein coefficients.

| Category | Function | $\Delta N_{\mathrm{bkg}}^{\mathrm{non-res}}$ | $\Delta N_{\mathrm{bkg}}^{\mathrm{non-res}}/N_{\mathrm{bkg}}^{\mathrm{non-res.}}$ [%] |
|---|---|---|---|
| 1 | $(1-x^{1/3})^b \cdot x^a$ | 5.5 | 2.4 |
| 2 | $\sum_{j=0}^{3} C_3^j x^j (1-x)^{3-j} b_{j,3}$ | 1.8 | 2.4 |
| 3 | $\exp(a \cdot x)$ | 0.6 | 3.6 |
| 4 | $\exp(a \cdot x)$ | 0.3 | 3.7 |
| 5 | $\exp(a \cdot x)$ | 1.6 | 2.8 |
| 6 | $\exp(a \cdot x)$ | 0.5 | 3.3 |
| 7 | $\exp(a \cdot x)$ | 0.3 | 5.1 |
| 8 | $\exp(a \cdot x)$ | 0.2 | 4.6 |
| 9 | $\exp(a \cdot x)$ | 1.5 | 2.3 |
| 10 | $\exp(a \cdot x)$ | 0.6 | 2.5 |
| 11 | $\exp(a \cdot x)$ | 0.4 | 5.6 |
| 12 | $\exp(a \cdot x)$ | 0.4 | 3.0 |

potential bias $\Delta N_{\mathrm{bkg}}^{\mathrm{non-res}}$ from the choice of the background modelling. A summary of the experimental and theoretical uncertainties with respect to the yield of the background from SM Higgs-boson processes, non-resonant background, and signal production is shown in Table 3.

The uncertainty in the combined 2015-2018 integrated luminosity is 1.7%. It is derived from the calibration of the luminosity scale using $x$-$y$ beam-separation scans, following a methodology similar to that detailed in Ref. [90], and using the LUCID-2 detector for the baseline luminosity measurements [91].

The efficiency of the diphoton trigger used to select events is evaluated in MC using a trigger matching technique and in data using a bootstrap method [92]. The uncertainty of the trigger efficiency for events in the diphoton invariant mass window of 105 GeV $< m_{\gamma\gamma} <$ 160 GeV is found to be 0.4%.

The uncertainty in vertex selection efficiency is assessed by comparing the efficiency of finding photon-pointing vertices in $Z \to e^+e^-$ events in data and MC [39]. The resulting uncertainty is found to be negligible in the inclusive category.

The systematic uncertainties due to the photon energy scale and resolution are obtained from Run 1 results [64], with minor updates in case of data-driven corrections using the full Run 2 dataset. The uncertainty in the energy scale has an effect below 1% on the normalization of the signals and SM Higgs background in the $p_{\mathrm{T}}$ range of the photons used in this analysis; the uncertainty in the energy resolution has an effect below 2% on the normalization of the signals and SM Higgs background. The uncertainties affecting the signal and SM Higgs background shapes due to the photon energy scale and resolution are evaluated.

Uncertainties in photon identification and isolation efficiencies are estimated, and their impact on the number of events in each category is quantified. The uncertainty in the photon identification efficiency [93] is calculated by varying the scale factor by its uncertainty for each photon in the simulation. The resulting uncertainty varies in the range of 1%–3% for SM Higgs background and 1%–2% for the signals in all

Table 3: Breakdown of the dominant systematic uncertainties. The uncertainties (in %) in the yield of signals, the background from SM Higgs-boson processes, and non-resonant background are shown. All production modes of the SM Higgs boson are considered together. A "–" indicates the systematic uncertainty is not applicable to the corresponding sample. If a given source has a different impact on the various categories, the given range corresponds to the smallest and largest impacts among categories or among the different signal models used in the analysis. In addition, the potential bias coming from non-resonant background modeling is shown relative to the background in the signal window [120, 130] GeV.

| Source | Signals [%] | Backgrounds [%] | |
|---|---|---|---|
| | | SM Higgs boson | Non-resonant background |
| Experimental | | | |
| Luminosity | 1.7 | | – |
| Jets (Scale, Resolution, JVT) | 0.2–3.3 | 0.9–30.7 | – |
| Electron/Photon (Scale, Resolution) | 0.3–1.5 | 0.6–2.7 | – |
| Photon (identification, isolation, trigger) | 2.2–2.6 | 2.8–4.3 | – |
| Electron (identification isolation) | 0.0–0.5 | 0.0–0.6 | – |
| Muon (identification, isolation, Scale, Resolution) | $< 0.6$ | $< 0.3$ | – |
| $E_{\mathrm{T}}^{\mathrm{miss}}$ reconstruction (jets, soft term) | $< 0.7$ | 0.4–13.9 | – |
| Pileup reweighting | 0.3–1.8 | 1.3–15 | – |
| Non-resonant background modelling | – | | 2–6 |
| Theoretical | | | |
| Factorization and renormalization scale | $< 1$ | 3.7–5.9 | – |
| PDF+$\alpha_{\mathrm{S}}$ | $< 6.6$ | 2.1–2.9 | – |
| Multiple parton-parton interactions | $< 1$ | | – |
| BR($H \rightarrow \gamma\gamma$) | 1.73 | | – |

categories. The uncertainty in the photon calorimeter isolation efficiency is calculated from efficiency differences between applying and not applying corrections derived from inclusive photon events to the isolation variables in simulation. The measurements of the efficiency correction factors using inclusive photon events are used to derive the efficiency uncertainty in the photon track isolation uncertainty. The photon isolation efficiency uncertainty is found to be in the range of 1%–3% for the SM Higgs background and 1%–2% for the signals.

Migration of events among categories occurs because of changes in the energy of identified particles, jets and the $E_{\mathrm{T}}^{\mathrm{miss}}$. The uncertainties in jet energy scale, resolution and jet vertex tagger are propagated to the $E_{\mathrm{T}}^{\mathrm{miss}}$ calculation. In addition, the uncertainties in the scale and resolution of the $E_{\mathrm{T}}^{\mathrm{miss}}$ soft term are estimated using the method described in Ref. [94]. The overall jet and $E_{\mathrm{T}}^{\mathrm{miss}}$ uncertainties in the SM Higgs-boson processes vary from 0.9% to 30.7% for each category. For signal processes, the overall jet and $E_{\mathrm{T}}^{\mathrm{miss}}$ uncertainties range from 0.2% to 3.3%. An uncertainty in the pileup modeling in MC simulation is accounted for. This results in an uncertainty of 0.3%–1.8% in the signal yield and 1.3%–1.5% in the SM Higgs-boson yield. The uncertainties related to the $b$-tagging of jets are typically less than 1.5% in the SM Higgs-boson yield used in "follow-up" analysis.

The predicted cross sections of the SM Higgs-boson and signal processes are affected by uncertainties due to missing higher-order terms in perturbative QCD. These uncertainties are estimated by varying the factorization and renormalization scales up and down from their nominal values by a factor of two, recalculating the cross section in each case, and taking the largest deviation from the nominal cross section as the uncertainty. The acceptance uncertainty related to the renormalization and factorization scales is less than 1% for signal and 2.8%–4.1% for the SM Higgs-boson processes [54]. For the signal processes, the effect of PDF+$\alpha_{\mathrm{S}}$ uncertainties in the acceptance times selection efficiency is below 5.9%. It is estimated using the recommendations of PDF4LHC [54]. Both intra-PDF and inter-PDF uncertainties are extracted. Intra-PDF uncertainties are obtained by varying the parameters of the NNPDF3.0LO PDF set, while inter-PDF uncertainties are estimated using alternative PDF sets (CT14 [95] at LO and MMHT2014 [96] at LO). The final inter-PDF uncertainty is the maximum deviation among all the variations from the central value obtained using the NNPDF3.0LO PDF set. In the case of the SM Higgs-boson processes, the acceptance effect of $\alpha_{\mathrm{S}}$ and the choice of PDFs range from 0.3% to 1.8%, which are taken from Ref. [54]. The uncertainty in the branching fraction of $h \to \gamma\gamma$ is 1.73%. The uncertainty in the effect of multiple parton–parton interactions is estimated by switching them on and off in Pythia in the production of the ggF SM Higgs-boson and signal samples. The resulting uncertainty in the number of events in this sample conservatively reaches 1% for all the categories.

## 8 Results

The results for the analysis are derived from an unbinned likelihood fit of the $m_{\gamma\gamma}$ distributions in the range 105 GeV $< m_{\gamma\gamma} <$ 160 GeV in each category simultaneously. The SM Higgs boson mass is set to 125.09 GeV [97]. The impact of the SM Higgs-boson mass uncertainty is negligible. The signal strength and the background shape parameters are set to be free parameters. The SM Higgs yields are taken from the SM predictions as discussed in Section 3. The systematic uncertainty of each nuisance parameter is taken into account by multiplying the likelihood by a Gaussian penalty function centered on the nominal value of this parameter with a width set to its uncertainty. The nominal value of each SM Higgs-boson background nuisance parameter (including its yield) is taken from the simulation normalized to the SM theoretical predictions.

Figures 4, 5 and 6 show the $m_{\gamma\gamma}$ distribution as well as the analytical signal-plus-background fits, for all twelve signal categories. The total background contains the non-resonant background and the predicted SM Higgs boson contribution. The fit results including the $\tilde{\chi}_1^{\pm}\tilde{\chi}_2^0 \to W^{\pm}\tilde{\chi}_1^0 h\tilde{\chi}_1^0$ signal with $m(\tilde{\chi}_1^{\pm}/\tilde{\chi}_2^0) = 200$ GeV, $m(\tilde{\chi}_1^0) = 0.5$ GeV, SM Higgs boson and non-resonant background are shown as the solid blue curves. A small excess of around two standard deviations is seen in category 4, which is consistent with the statistical fluctuation as well as the SM Higgs prediction.

The event yields in the range of 120 GeV $< m_{\gamma\gamma} <$ 130 GeV for data, the signal models, the SM Higgs-boson background and non-resonant background in the twelve categories are shown in Table 4. The signal samples shown correspond to $\tilde{\chi}_1^{\pm}\tilde{\chi}_2^0 \to W^{\pm}\tilde{\chi}_1^0 h\tilde{\chi}_1^0$ signal with $m(\tilde{\chi}_1^{\pm}/\tilde{\chi}_2^0) = 200$ GeV, $m(\tilde{\chi}_1^0) = 0.5$ GeV, and $h\tilde{G}Z\tilde{G}$, $h\tilde{G}h\tilde{G}$ signal with $m(\tilde{\chi}_1^0) = 150$ GeV, $m(\tilde{G}) = 1$ MeV. The yields for the non-resonant background and SM Higgs-boson are obtained from a simultaneous background-only fit of the full data spectrum for the twelve categories. The yields for the signals are estimated from the simulation. The uncertainties correspond to the quadrature sum of the statistical and systematic uncertainties. For all the categories, data and background prediction agree well within the statistical and systematic uncertainties.

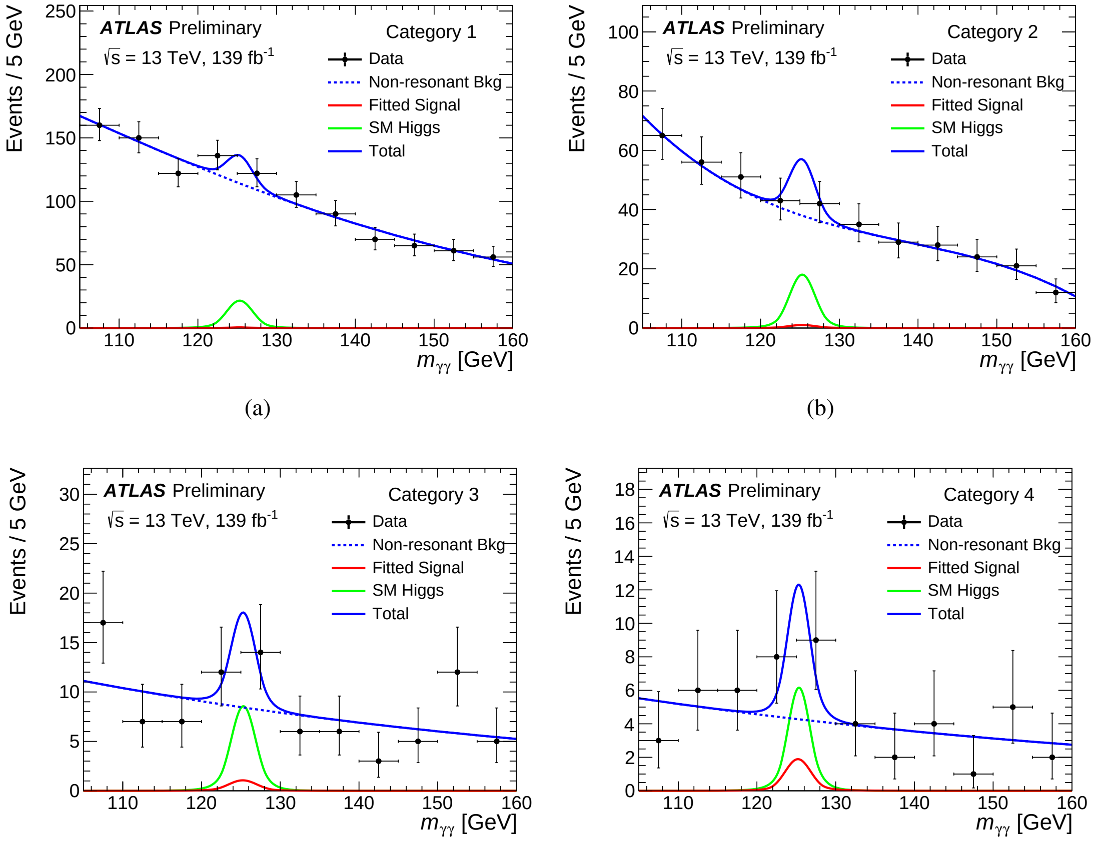

(a)

(b)

(c)

(d)

Figure 4: Diphoton invariant mass spectra from data and the corresponding fitted signal and background in leptonic categories (a) 1, (b) 2, (c) 3, and (d) 4. The signal samples shown correspond to $\tilde{\chi}_1^{\pm}\tilde{\chi}_2^0 \rightarrow W^{\pm}\tilde{\chi}_1^0 h\tilde{\chi}_1^0$ signal with $m(\tilde{\chi}_1^{\pm}/\tilde{\chi}_2^0) = 200$ GeV, $m(\tilde{\chi}_1^0) = 0.5$ GeV. The non-resonant background (blue-dashed curve), the SM Higgs boson (green-solid curve), and the signal (red-solid curve) are obtained from a simultaneous signal-plus-background fit of the full data spectrum for the twelve categories. The total of these contributions is shown by the blue-solid curves.

The fitted $m_{\gamma\gamma}$ distributions for the "follow-up" signal regions are shown in Figure 7. No significant excess of events is seen in any of the two regions. In 'SR1L$\gamma\gamma$-a', two events are observed with $3.1 \pm 0.8$ non-resonant background and $0.5^{+0.2}_{-0.4}$ SM Higgs boson events expected in the $m_{\gamma\gamma}$ range (120 GeV–130 GeV). In case of 'SR1L$\gamma\gamma$-b', 31 events are observed, where there are $16.6 \pm 1.9$ events from non-resonant background and $8.6^{+1.3}_{-2.1}$ from the SM Higgs boson contributions expected in the $m_{\gamma\gamma}$ range (120 GeV–130 GeV).

## 8.1 Limits on the visible cross section

The observed yields agree with the background predictions, as shown in Table 4, and no significant excess of events is observed. Upper limits are set on the visible cross section $\sigma_{\text{vis}}^{\text{BSM}} \equiv (\mathcal{A} \times \epsilon \times \sigma)^{\text{BSM}}$ for the beyond Standard Model (BSM) physics processes producing $E_{\text{T}}^{\text{miss}}$ and an SM Higgs boson decaying into two photons, where $\mathcal{A}$ and $\epsilon$ are the acceptance and the efficiency of the signal, respectively. The SM background prediction is excluded from this BSM visible cross section. These are extracted by performing

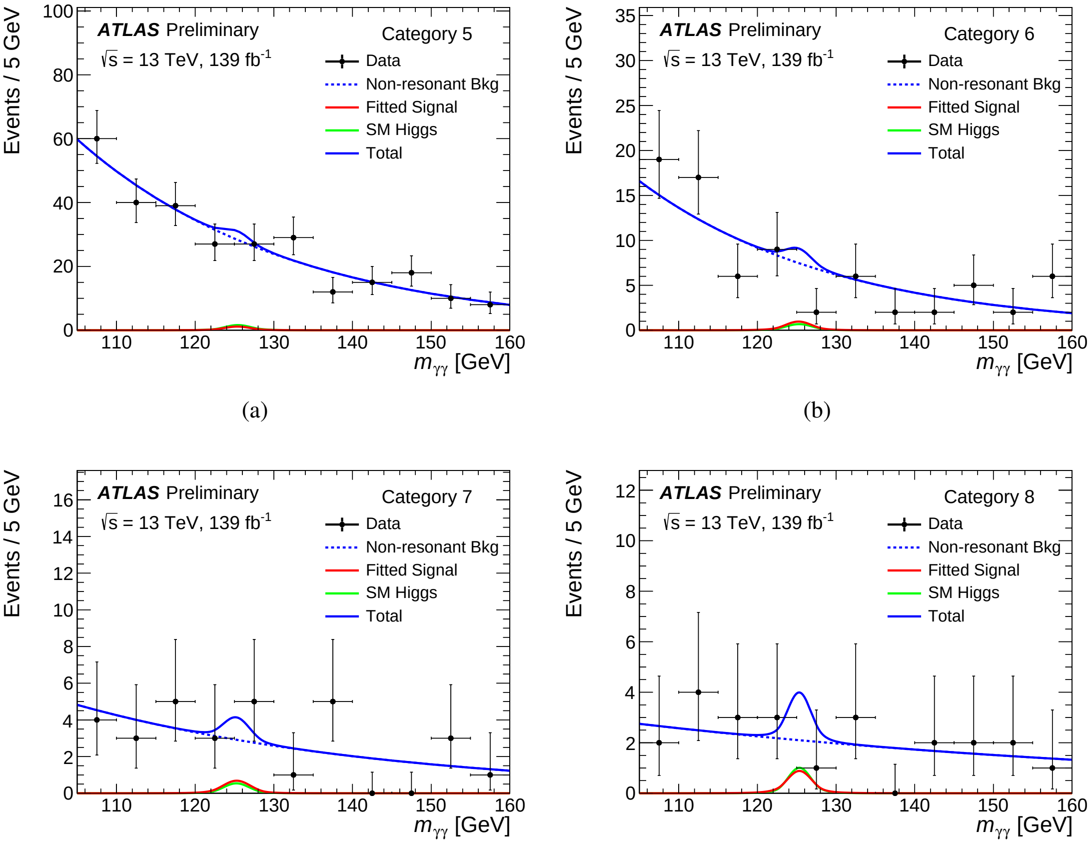

(a)

(b)

(c)

(d)

Figure 5: Diphoton invariant mass spectra from data and the corresponding fitted signal and background in hadronic categories (a) 5, (b) 6, (c) 7, and (d) 8. The signal samples shown correspond to $\tilde{\chi}_1^\pm\tilde{\chi}_2^0 \rightarrow W^\pm\tilde{\chi}_1^0 h\tilde{\chi}_1^0$ signal with $m(\tilde{\chi}_1^\pm/\tilde{\chi}_2^0)$ = 200 GeV, $m(\tilde{\chi}_1^0)$ = 0.5 GeV. The non-resonant background (blue-dashed curve), the SM Higgs boson (green-solid curve), and the signal (red-solid curve) are obtained from a simultaneous signal-plus-background fit of the full data spectrum for the twelve categories. The total of these contributions is shown by the blue-solid curves.

a fit to the non-resonant background and SM Higgs background, individually for each category, each time injecting a signal with the same mass distribution as the SM Higgs but with a free normalization. Figure 8 shows the observed and expected 95% confidence level (CL) upper limits on $\sigma_{\text{vis}}^{\text{BSM}}$ for each of the 12 different categories defined in this analysis, which are calculated using a one-sided profile-likelihood ratio and the CL$_\text{s}$ formalism [98] with the asymptotic approximation in Ref. [99]. The same parameterizations for the BSM signal and the total SM Higgs-boson background are used in each of the 12 different categories. The statistical uncertainty is dominant for all the categories.

## 8.2 Interpretation of Wino-like $\tilde{\chi}_1^\pm\tilde{\chi}_2^0 \rightarrow W^\pm\tilde{\chi}_1^0 h\tilde{\chi}_1^0$ model

Since no significant excess is observed, fit results are interpreted in terms of 95% CL exclusion limits on the model's production cross-section. Upper limits on the contribution of events from new physics are computed by using the modified frequentist approach CL$_s$ based on asymptotic formulas. Figure. 9 shows 95% CL exclusion limits on the production cross section of $\tilde{\chi}_1^\pm\tilde{\chi}_2^0 \rightarrow W^\pm\tilde{\chi}_1^0 h\tilde{\chi}_1^0$ as a function of

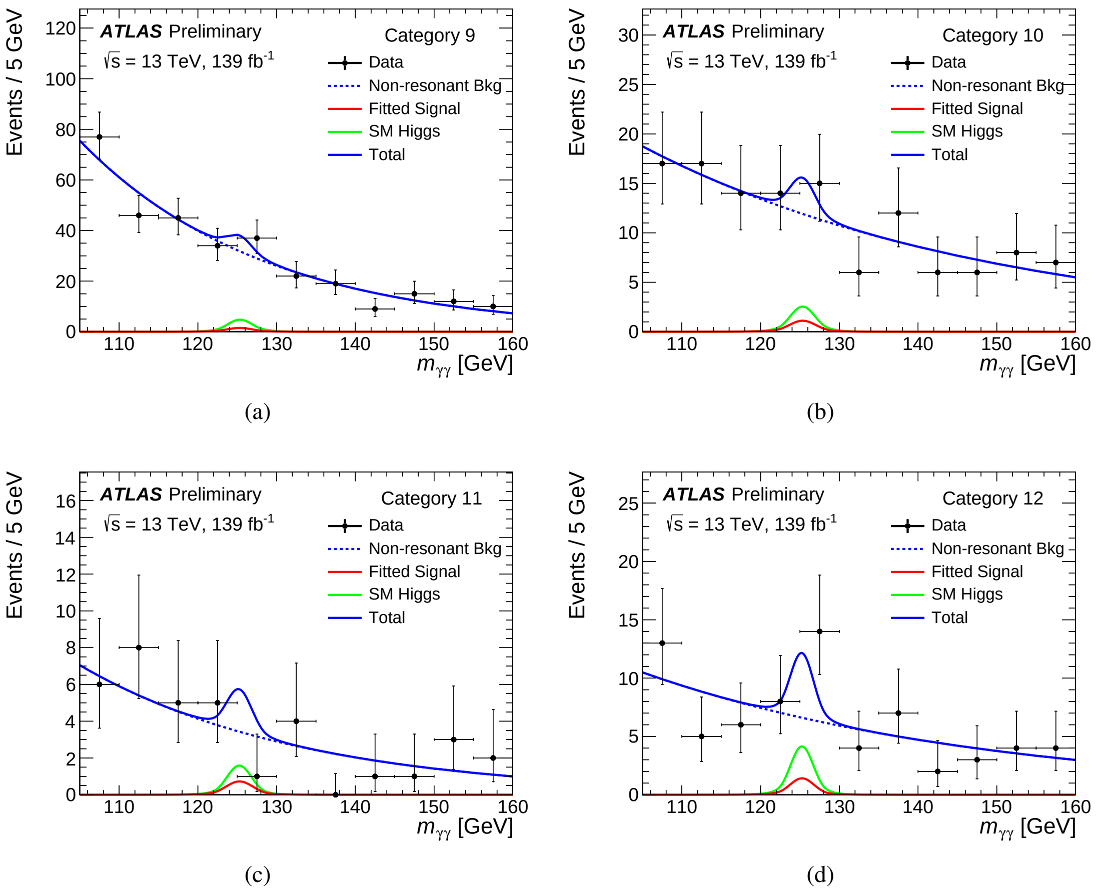

Figure 6: Diphoton invariant mass spectra from data and the corresponding fitted signal and background in rest categories (a) 9, (b) 10, (c) 11, and (d) 12. The signal samples shown correspond to $\tilde{\chi}_1^{\pm}\tilde{\chi}_2^0 \to W^{\pm}\tilde{\chi}_1^0 h\tilde{\chi}_1^0$ signal with $m(\tilde{\chi}_1^{\pm}/\tilde{\chi}_2^0) = 200$ GeV, $m(\tilde{\chi}_1^0) = 0.5$ GeV. The non-resonant background (blue-dashed curve), the SM Higgs boson (green-solid curve), and the signal (red-solid curve) are obtained from a simultaneous signal-plus-background fit of the full data spectrum for the twelve categories. The total of these contributions is shown by the blue-solid curves.

$m(\tilde{\chi}_1^{\pm}/\tilde{\chi}_2^0)$. The observed 95% CL upper limits on the production cross section vary from 1.92 pb to 0.16 pb for $m(\tilde{\chi}_1^{\pm}/\tilde{\chi}_2^0)$ from 150 GeV to 600 GeV. The expected 95% CL upper limits range from 1.43 pb to 0.11 pb. The 95% CL lower limit of 315 GeV in $m(\tilde{\chi}_1^{\pm}/\tilde{\chi}_2^0)$, where $m(\tilde{\chi}_1^0)$ is 0.5 GeV, is set. The observed and expected exclusion contours at 95% CL for $\tilde{\chi}_1^{\pm}\tilde{\chi}_2^0$ production in the $m(\tilde{\chi}_1^{\pm}/\tilde{\chi}_2^0)$–$m(\tilde{\chi}_1^0)$ plane are shown in Figure 10 (a). This result is shown together with previous exclusion limits in the same channel, or in related channels, in Figure 10 (b). The result presented here is a significant improvement with respect to previous diphoton results.

### 8.3 Interpretation of the Higgsino-like $h\tilde{G}Z\tilde{G}$, $h\tilde{G}h\tilde{G}$ model

As a second SUSY scenario, a GMSB model where two lightest neutralinos and the lightest chargino are Higgsinos is considered [32–34]. The $\tilde{\chi}_1^{\pm}$, $\tilde{\chi}_1^0$, $\tilde{\chi}_2^0$, are almost mass degenerate in this model with $\tilde{\chi}_1^0$ as the lightest of the three states. The LSP is a gravitino. In Figure 11, the observed and expected 95% CL upper limits, with uncertainties, on the Higgsino production cross section in the channels of $h\tilde{G}Z\tilde{G}$, $h\tilde{G}h\tilde{G}$

Table 4: Event yields in the range of 120 GeV < $m_{\gamma\gamma}$ < 130 GeV for data, the signal models, the SM Higgs-boson background and non-resonant background in each analysis category, for an integrated luminosity of 139 $\text{fb}^{-1}$. The signal samples shown correspond to $\tilde{\chi}_1^\pm\tilde{\chi}_2^0 \to W^\pm\tilde{\chi}_1^0 h\tilde{\chi}_1^0$ signal with $m(\tilde{\chi}_1^\pm/\tilde{\chi}_2^0) = 200$ GeV, $m(\tilde{\chi}_1^0) = 0.5$ GeV, and $h\tilde{G}Z\tilde{G}$, $h\tilde{G}h\tilde{G}$ signal with $m(\tilde{\chi}_1^0) = 150$ GeV, $m(\tilde{G}) = 1$ MeV. The yields for the non-resonant background and SM Higgs-boson are obtained from a simultaneous background-only fit of the full data spectrum for the twelve categories. The yields for the signals are estimated from the simulation. The uncertainties correspond to the quadrature sum of the statistical and systematic uncertainties.

| Category | Data | Total bkg. | Non-resonant bkg. | SM Higgs boson | $W^\pm\tilde{\chi}_1^0 h\tilde{\chi}_1^0$ | $h\tilde{G}Z\tilde{G}$ | $h\tilde{G}h\tilde{G}$ |
|---|---|---|---|---|---|---|---|
| 1 | 258 | 246 ± 7 | 230 ± 7 | 16.3 ± 1.4 | 2.8 ± 0.6 | 5 ± 6 | 5 ± 7 |
| 2 | 85 | 93 ± 4 | 77 ± 4 | 15.6 ± 1.3 | 6.6 ± 1.5 | 6 ± 7 | 4 ± 6 |
| 3 | 26 | 24.1 ± 2.0 | 17.1 ± 1.9 | 7.0 ± 0.6 | 6.9 ± 1.5 | 1.8 ± 2.2 | 1.8 ± 2.6 |
| 4 | 17 | 12.8 ± 1.4 | 8.4 ± 1.3 | 4.4 ± 0.4 | 10.7 ± 2.4 | 0.8 ± 0.8 | 0.9 ± 1.3 |
| 5 | 54 | 60 ± 4 | 57.9 ± 3.5 | 1.9 ± 0.6 | 7.2 ± 1.6 | 2.4 ± 2.8 | 0.8 ± 1.2 |
| 6 | 11 | 16.1 ± 1.8 | 15.4 ± 1.8 | 0.74 ± 0.26 | 6.0 ± 1.3 | 1.0 ± 1.2 | 0.4 ± 0.5 |
| 7 | 8 | 6.3 ± 1.1 | 5.9 ± 1.1 | 0.42 ± 0.10 | 4.3 ± 1.0 | 0.6 ± 0.8 | 0.18 ± 0.26 |
| 8 | 4 | 5.2 ± 1.0 | 4.4 ± 1.0 | 0.80 ± 0.11 | 5.3 ± 1.2 | 0.8 ± 1.0 | 0.20 ± 0.28 |
| 9 | 71 | 69 ± 4 | 65 ± 4 | 3.9 ± 0.8 | 9.1 ± 2.0 | 3 ± 4 | 1.1 ± 1.5 |
| 10 | 29 | 26.3 ± 2.2 | 24.2 ± 2.2 | 2.1 ± 0.4 | 6.9 ± 1.5 | 2.4 ± 2.8 | 0.5 ± 0.7 |
| 11 | 6 | 8.6 ± 1.2 | 7.2 ± 1.2 | 1.40 ± 0.22 | 4.6 ± 1.0 | 1.6 ± 2.0 | 0.3 ± 0.5 |
| 12 | 22 | 16.6 ± 1.7 | 13.4 ± 1.7 | 3.15 ± 0.33 | 7.9 ± 1.8 | 4 ± 5 | 0.5 ± 0.6 |

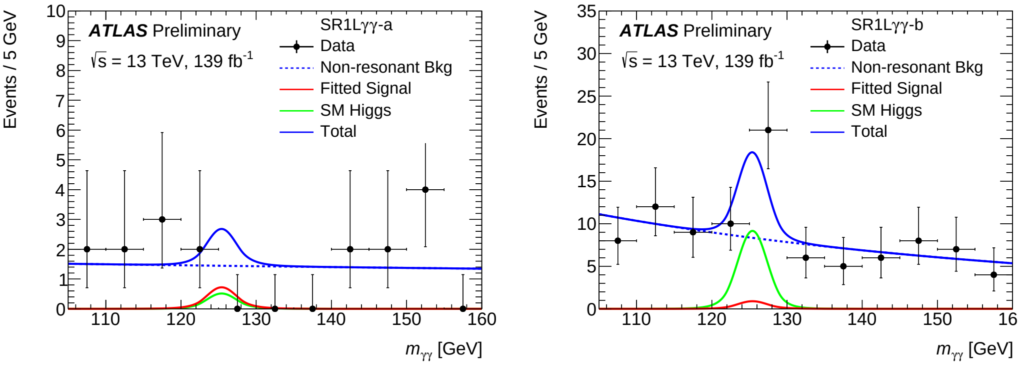

(a) (b)

Figure 7: Diphoton invariant mass spectra from data and the corresponding fitted signal and background in the signal regions (a) ‘SR1L$\gamma\gamma$-a’ and (b) ‘SR1L$\gamma\gamma$-b’ . The signal samples shown correspond to $\tilde{\chi}_1^\pm\tilde{\chi}_2^0 \to W^\pm\tilde{\chi}_1^0 h\tilde{\chi}_1^0$ signal with $m(\tilde{\chi}_1^\pm/\tilde{\chi}_2^0) = 200$ GeV, $m(\tilde{\chi}_1^0) = 0.5$ GeV. The non-resonant background (blue-dashed curve), the SM Higgs boson (green-solid curve), and the signal (red-solid curve) are obtained from a signal-plus-background fit of the full data spectrum in ‘SR1L$\gamma\gamma$-a’ (a) and ‘SR1L$\gamma\gamma$-b’ (b) separately. The total of these contributions is shown by the blue-solid curves.

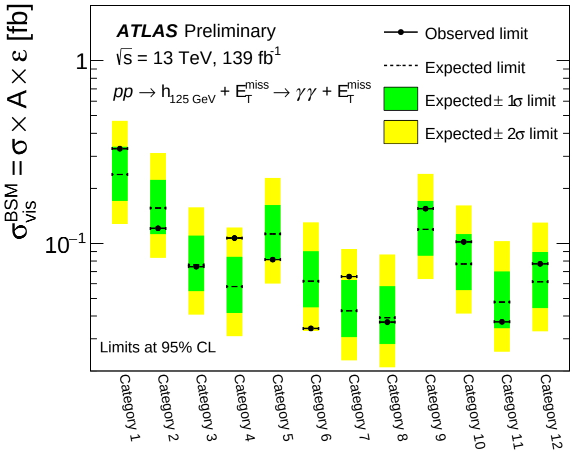

Figure 8: The 95% CL model-independent upper limits on the visible cross section $\sigma_{\text{vis}}^{\text{BSM}} = \sigma \times A \times \epsilon$ for any $pp \to h(125\text{ GeV}) + E_{\text{T}}^{\text{miss}} \to \gamma\gamma + E_{\text{T}}^{\text{miss}}$ processes of beyond the standard model (BSM), for each of the 12 different categories defined in this analysis.

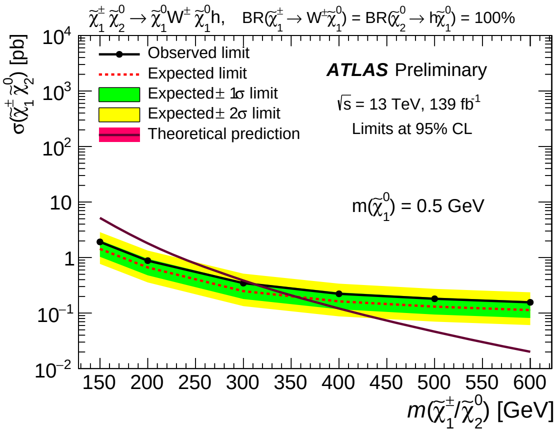

Figure 9: Expected and observed 95% CL exclusion upper limits on the production cross section of $\tilde{\chi}_1^{\pm}\tilde{\chi}_2^0 \to W^{\pm}\tilde{\chi}_1^0 h\tilde{\chi}_1^0$ as a function of $m(\tilde{\chi}_1^{\pm}/\tilde{\chi}_2^0)$.

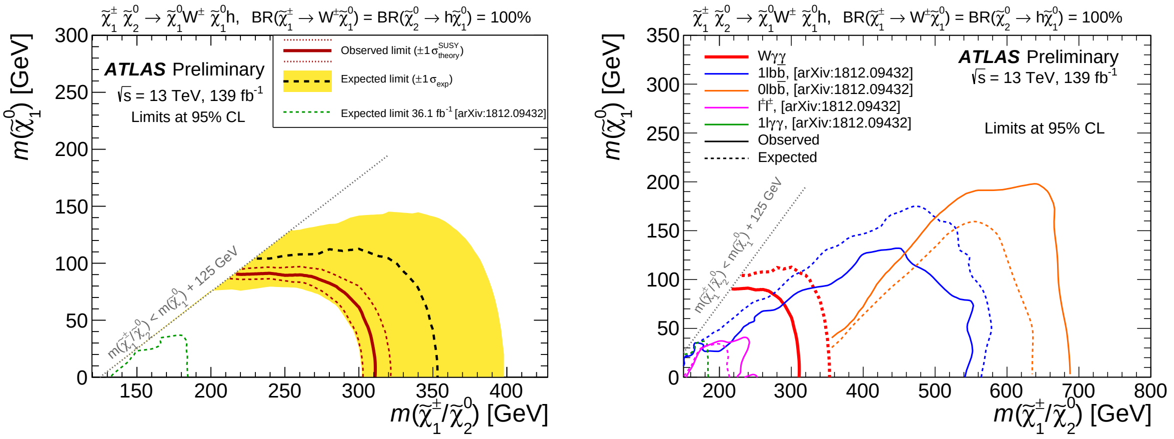

(a)

(b)

Figure 10: (a): The observed (red solid line) and expected (black dashed line) exclusion limit contours at 95% CL for $\tilde{\chi}_1^\pm\tilde{\chi}_2^0$ production in the $(m(\tilde{\chi}_1^\pm/\tilde{\chi}_2^0), m(\tilde{\chi}_1^0))$ plane. The red dashed lines represent the $\pm1\sigma$ theoretical uncertainty for the observed limit. The $\pm1\sigma$ expected exclusion limit contour is shown as the yellow band. The expected limit for the 36.1 fb$^{-1}$ analysis [29] is also shown for comparison in the green dashed line. (b): Comparison of the expected and observed exclusions (red dashed and solid line) for this analysis and each previous analysis [29].

for different $m(\tilde{\chi}_1^0)$ masses are presented. The theoretical prediction includes the $\tilde{\chi}_1^0\,\tilde{\chi}_2^0$, $\tilde{\chi}_1^0\,\tilde{\chi}_1^\pm$, $\tilde{\chi}_2^0\,\tilde{\chi}_1^\pm$, and $\tilde{\chi}_1^\pm\,\tilde{\chi}_1^\mp$ production modes, where all Higgsinos promptly decay to the $\tilde{\chi}_1^0$ and particles that have too low momentum to be detected. The observed 95% CL upper limits on the production cross section are set from 7.13 pb to 0.20 pb for Higgsino mass between 130 GeV and 800 GeV in the scenario of $h\tilde{G}Z\tilde{G}$, and 17.3 pb to 0.19 pb for the case of $\tilde{G}h\tilde{G}$.

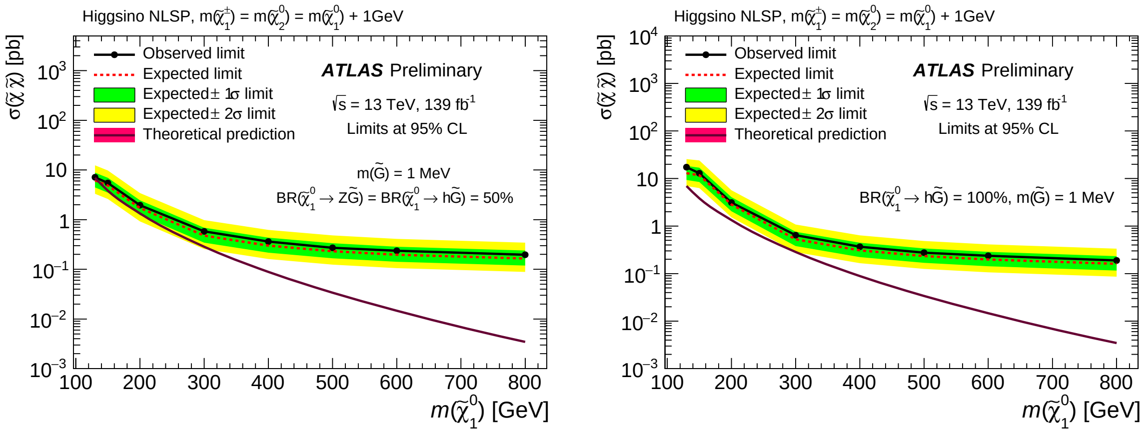

(a)

(b)

Figure 11: Expected and observed 95% CL exclusion upper limits on the Higgsino production ($\tilde{\chi}\tilde{\chi} \equiv \tilde{\chi}_1^0\tilde{\chi}_2^0, \tilde{\chi}_1^0\tilde{\chi}_1^\pm, \tilde{\chi}_2^0\tilde{\chi}_1^\pm, \tilde{\chi}_1^\pm\tilde{\chi}_1^\mp$) cross section in the channels of (a) $h\tilde{G}Z\tilde{G}$, (b) $h\tilde{G}h\tilde{G}$ as a function of the Higgsino mass. The theoretical prediction includes the $\tilde{\chi}_1^0\,\tilde{\chi}_2^0$, $\tilde{\chi}_1^0\,\tilde{\chi}_1^\pm$, $\tilde{\chi}_2^0\,\tilde{\chi}_1^\pm$, and $\tilde{\chi}_1^\pm\,\tilde{\chi}_1^\mp$ production modes, where all Higgsinos promptly decay to the $\tilde{\chi}_1^0$ and particles that have too low momentum to be detected.

## 9 Conclusion

A search for a chargino and a neutralino decaying via the 125 GeV Higgs boson into photons is presented. This study is based on the full Run 2 data collected between 2015 and 2018 with the ATLAS detector at the LHC, corresponding to an integrated luminosity of 139 $\text{fb}^{-1}$ of $pp$ collisions at a centre-of-mass energy of 13 TeV. No significant excess over the expected background is observed. Upper limits at 95% confidence level are set on the $\tilde{\chi}_1^{\pm}\tilde{\chi}_2^0$ and Higgsino production cross section, and the visible cross section for beyond the Standard Model physics processes. For the model of $\tilde{\chi}_1^{\pm}\tilde{\chi}_2^0 \rightarrow W^{\pm}\tilde{\chi}_1^0 h\tilde{\chi}_1^0$, the observed 95% confidence-level upper limits on the production cross section vary from 1.92 pb to 0.16 pb for $m(\tilde{\chi}_1^{\pm}/\tilde{\chi}_2^0)$ from 150 GeV to 600 GeV. The expected 95% confidence-level upper limits range from 1.43 pb to 0.11 pb. The 95% confidence-level lower limit of 315 GeV in $m(\tilde{\chi}_1^{\pm}/\tilde{\chi}_2^0)$, where $m(\tilde{\chi}_1^0)$ is 0.5 GeV, is set. For the Higgsino production, the observed 95% confidence-level upper limits on the production cross section are set from 7.13 pb to 0.20 pb for Higgsino masses between 130 GeV and 800 GeV in the scenario of $h\tilde{G}Z\tilde{G}$, and 17.3 pb to 0.19 pb for the case of $h\tilde{G}h\tilde{G}$. No significant excess over the expected background is observed in the “follow-up” analysis using this full Run 2 data.

## References

[1] ATLAS Collaboration, *Observation of a new particle in the search for the Standard Model Higgs boson with the ATLAS detector at the LHC*, Phys. Lett. B **716** (2012) 1, arXiv: `1207.7214 [hep-ex]`.

[2] CMS Collaboration, *Observation of a new boson at a mass of 125 GeV with the CMS experiment at the LHC*, Phys. Lett. B **716** (2012) 30, arXiv: `1207.7235 [hep-ex]`.

[3] ATLAS and CMS Collaborations, *Combined Measurement of the Higgs Boson Mass in pp Collisions at $\sqrt{s} = 7$ and 8 TeV with the ATLAS and CMS Experiments*, Phys. Rev. Lett. **114** (2015) 191803, arXiv: `1503.07589 [hep-ex]`.

[4] ATLAS and CMS Collaborations, *Measurements of the Higgs boson production and decay rates and constraints on its couplings from a combined ATLAS and CMS analysis of the LHC pp collision data at $\sqrt{s} = 7$ and 8 TeV*, JHEP **08** (2016) 045, arXiv: `1606.02266 [hep-ex]`.

[5] N. Sakai, *Naturalness in Supersymmetric Guts*, Z. Phys. C **11** (1981) 153.

[6] S. Dimopoulos, S. Raby, and F. Wilczek, *Supersymmetry and the Scale of Unification*, Phys. Rev. D **24** (1981) 1681.

[7] L. E. Ibanez and G. G. Ross, *Low-Energy Predictions in Supersymmetric Grand Unified Theories*, Phys. Lett. B **105** (1981) 439.

[8] S. Dimopoulos and H. Georgi, *Softly Broken Supersymmetry and SU(5)*, Nucl. Phys. B **193** (1981) 150.

[9] Yu. A. Golfand and E. P. Likhtman, *Extension of the Algebra of Poincare Group Generators and Violation of p Invariance*, JETP Lett. **13** (1971) 323, [Pisma Zh. Eksp. Teor. Fiz. **13** (1971) 452].

[10] D. V. Volkov and V. P. Akulov, *Is the Neutrino a Goldstone Particle?* Phys. Lett. B **46** (1973) 109.

[11] J. Wess and B. Zumino, *Supergauge Transformations in Four-Dimensions*, Nucl. Phys. B **70** (1974) 39.

[12] J. Wess and B. Zumino, *Supergauge Invariant Extension of Quantum Electrodynamics*, Nucl. Phys. B **78** (1974) 1.

[13] S. Ferrara and B. Zumino, *Supergauge Invariant Yang-Mills Theories*, Nucl. Phys. B **79** (1974) 413.

[14] A. Salam and J. A. Strathdee, *Supersymmetry and Nonabelian Gauges*, Phys. Lett. B **51** (1974) 353.

[15] H. Goldberg, *Constraint on the Photino Mass from Cosmology*, Phys. Rev. Lett. **50** (1983) 1419, Erratum: *Constraint on the Photino Mass from Cosmology*, Phys. Rev. Lett. **103** (2009) 099905.

[16] J. R. Ellis, J. S. Hagelin, D. V. Nanopoulos, K. A. Olive, and M. Srednicki, *Supersymmetric Relics from the Big Bang*, Nucl. Phys. B **238** (1984) 453.

[17] G. R. Farrar and P. Fayet, *Phenomenology of the Production, Decay, and Detection of New Hadronic States Associated with Supersymmetry*, Phys. Lett. B **76** (1978) 575.

[18] M. Dine and W. Fischler, *A Phenomenological Model of Particle Physics Based on Supersymmetry*, Phys. Lett. B **110** (1982) 227.

[19] L. Alvarez-Gaume, M. Claudson, and M. B. Wise, *Low-Energy Supersymmetry*, Nucl. Phys. B **207** (1982) 96.

[20] C. R. Nappi and B. A. Ovrut, *Supersymmetric Extension of the SU(3) x SU(2) x U(1) Model*, Phys. Lett. B **113** (1982) 175.

[21] R. Barbieri and G. F. Giudice, *Upper Bounds on Supersymmetric Particle Masses*, Nucl. Phys. B **306** (1988) 63.

[22] B. de Carlos and J. A. Casas, *One loop analysis of the electroweak breaking in supersymmetric models and the fine tuning problem*, Phys. Lett. B **309** (1993) 320, arXiv: `hep-ph/9303291`.

[23] P. Fayet, *Supersymmetry and Weak, Electromagnetic and Strong Interactions*, Phys. Lett. B **64** (1976) 159.

[24] P. Fayet, *Spontaneously Broken Supersymmetric Theories of Weak, Electromagnetic and Strong Interactions*, Phys. Lett. B **69** (1977) 489.

[25] S. P. Das, M. Guchait, and D. P. Roy, *Testing SUSY models for the muon g-2 anomaly via chargino-neutralino pair production at the LHC*, Phys. Rev. D **90** (2014) 055011, arXiv: `1406.6925 [hep-ph]`.

[26] M. A. Ajaib, B. Dutta, T. Ghosh, I. Gogoladze, and Q. Shafi, *Neutralinos and sleptons at the LHC in light of muon* $(g-2)_\mu$, Phys. Rev. D **92** (2015) 075033, arXiv: `1505.05896 [hep-ph]`.

[27] M. Chakraborti, U. Chattopadhyay, A. Choudhury, A. Datta, and S. Poddar, *Reduced LHC constraints for higgsino-like heavier electroweakinos*, JHEP **11** (2015) 050, arXiv: `1507.01395 [hep-ph]`.

[28] M. Endo, K. Hamaguchi, S. Iwamoto, and K. Yanagi, *Probing minimal SUSY scenarios in the light of muon* $g-2$ *and dark matter*, JHEP **06** (2017) 031, arXiv: `1704.05287 [hep-ph]`.

[29] ATLAS Collaboration, *Search for chargino and neutralino production in final states with a Higgs boson and missing transverse momentum at* $\sqrt{s} = 13$ *TeV with the ATLAS detector*, CERN-EP-2018-306 (2018), arXiv: `1812.09432 [hep-ex]`.

[30] J. Alwall, P. Schuster, and N. Toro, *Simplified Models for a First Characterization of New Physics at the LHC*, Phys. Rev. D **79** (2009) 075020, arXiv: `0810.3921 [hep-ph]`.

[31] D. Alves et al., *Simplified Models for LHC New Physics Searches*, J. Phys. G **39** (2012) 105005, arXiv: `1105.2838 [hep-ph]`.

[32] CMS Collaboration, *Searches for electroweak neutralino and chargino production in channels with Higgs, Z, and W bosons in pp collisions at 8 TeV*, Phys. Rev. D **90** (2014) 092007, arXiv: `1409.3168 [hep-ex]`.

[33] K. T. Matchev and S. D. Thomas, *Higgs and Z boson signatures of supersymmetry*, Phys. Rev. D **62** (2000) 077702, arXiv: `hep-ph/9908482 [hep-ph]`.

[34] J. T. Ruderman and D. Shih, *General Neutralino NLSPs at the Early LHC*, JHEP **08** (2012) 159, arXiv: `1103.6083 [hep-ph]`.

[35] ATLAS Collaboration, *The ATLAS Experiment at the CERN Large Hadron Collider*, JINST **3** (2008) S08003.

[36] ATLAS Collaboration, *ATLAS Insertable B-Layer Technical Design Report*, ATLAS-TDR-19 (2010), URL: `https://cds.cern.ch/record/1291633`; *ATLAS Insertable B-Layer Technical Design Report Addendum*, ATLAS-TDR-19-ADD-1 (2012), URL: `https://cds.cern.ch/record/1451888`.

[37] B. Abbott et al., *Production and Integration of the ATLAS Insertable B-Layer*, JINST **13** (2018) T05008, arXiv: `1803.00844 [physics.ins-det]`.

[38] ATLAS Collaboration, *Performance of the ATLAS trigger system in 2015*, Eur. Phys. J. C **77** (2017) 317, arXiv: `1611.09661 [hep-ex]`.

[39] ATLAS Collaboration, *Search for resonances in diphoton events at $\sqrt{s}$=13 TeV with the ATLAS detector*, JHEP **09** (2016) 001, arXiv: `1606.03833 [hep-ex]`.

[40] J. Alwall et al., *The automated computation of tree-level and next-to-leading order differential cross sections, and their matching to parton shower simulations*, JHEP **07** (2014) 79, arXiv: `1405.0301 [hep-ph]`.

[41] R. D. Ball et al., *Parton distributions for the LHC run II*, JHEP **04** (2015) 040, arXiv: `1410.8849 [hep-ph]`.

[42] T. Sjostrand, S. Mrenna, and P. Skands, *A brief introduction to PYTHIA 8.1*, Comput. Phys. Commun. **178** (2008) 852, arXiv: `0710.3820 [hep-ph]`.

[43] ATLAS Collaboration, *ATLAS Pythia 8 tunes to* 7 *TeV data*, ATL-PHYS-PUB-2014-021, 2014, URL: `https://cds.cern.ch/record/1966419`.

[44] NNPDF Collaboration, R. D. Ball et al., *Parton distributions with LHC data*, Nucl. Phys. B **867** (2013) 244, arXiv: `1207.1303 [hep-ph]`.

[45] P. Nason, *A new method for combining NLO QCD with shower Monte Carlo algorithms*, JHEP **11** (2004) 040, arXiv: `hep-ph/0409146`.

[46] S. Alioli, P. Nason, C. Oleari, and E. Re, *NLO Higgs boson production via gluon fusion matched with shower in POWHEG*, JHEP **04** (2009) 002, arXiv: `0812.0578 [hep-ph]`.

[47] P. Nason and C. Oleari, *NLO Higgs boson production via vector-boson fusion matched with shower in POWHEG*, JHEP **02** (2010) 037, arXiv: `0911.5299 [hep-ph]`.

[48] S. Alioli, P. Nason, C. Oleari, and E. Re, *A general framework for implementing NLO calculations in shower Monte Carlo programs: the POWHEG BOX*, JHEP **06** (2010) 043, arXiv: `1002.2581 [hep-ph]`.

[49] ATLAS Collaboration, *Example ATLAS tunes of* PYTHIA8, PYTHIA6 *and* POWHEG *to an observable sensitive to Z boson transverse momentum*, ATL-PHYS-PUB-2013-017, 2013, URL: `https://cds.cern.ch/record/1629317`.

[50] H.-L. Lai et al., *New parton distributions for collider physics*, Phys. Rev. D **82** (2010) 074024, arXiv: `1007.2241 [hep-ph]`.

[51] T. Gleisberg et al., *Event generation with SHERPA 1.1*, JHEP **02** (2009) 007, arXiv: `0811.4622 [hep-ph]`.

[52] S. Schumann and F. Krauss, *A Parton shower algorithm based on Catani-Seymour dipole factorisation*, JHEP **03** (2008) 038, arXiv: `0709.1027 [hep-ph]`.

[53] S. Höche, F. Krauss, S. Schumann, and F. Siegert, *QCD matrix elements and truncated showers*, JHEP **05** (2009) 053, arXiv: `0903.1219 [hep-ph]`.

[54] D. de Florian et al., *Handbook of LHC Higgs Cross Sections: 4. Deciphering the Nature of the Higgs Sector*, (2016), arXiv: `1610.07922 [hep-ph]`.

[55] G. Bozzi, B. Fuks, and M. Klasen, *Threshold Resummation for Slepton-Pair Production at Hadron Colliders*, Nucl. Phys. B **777** (2007) 157, arXiv: `hep-ph/0701202 [hep-ph]`.

[56] B. Fuks, M. Klasen, D. R. Lamprea, and M. Rothering, *Precision predictions for electroweak superpartner production at hadron colliders with Resummino*, Eur. Phys. J. C **73** (2013) 2480, arXiv: `1304.0790 [hep-ph]`.

[57] B. Fuks, M. Klasen, D. R. Lamprea, and M. Rothering, *Revisiting slepton pair production at the Large Hadron Collider*, JHEP **01** (2014) 168, arXiv: `1310.2621 [hep-ph]`.

[58] J. Fiaschi and M. Klasen, *Slepton pair production at the LHC in NLO+NLL with resummation-improved parton densities*, JHEP **03** (2018) 094, arXiv: `1801.10357 [hep-ph]`.

[59] C. Borschensky et al., *Squark and gluino production cross sections in pp collisions at* $\sqrt{s} = 13, 14, 33$ *and* $100$ *TeV*, Eur. Phys. J. C **74** (2014) 3174, arXiv: `1407.5066 [hep-ph]`.

[60] D. J. Lange, *The EvtGen particle decay simulation package*, Nucl. Instrum. Meth. A **462** (2001) 152.

[61] ATLAS Collaboration, *The Pythia 8 A3 tune description of ATLAS minimum bias and inelastic measurements incorporating the Donnachie–Landshoff diffractive model*, ATL-PHYS-PUB-2016-017, 2016, URL: `https://cds.cern.ch/record/2206965`.

[62] ATLAS Collaboration, *The ATLAS Simulation Infrastructure*, Eur. Phys. J. C **70** (2010) 823, arXiv: `1005.4568 [physics.ins-det]`.

[63] S. Agostinelli et al., *GEANT4 – A Simulation toolkit*, Nucl. Instrum. Meth. A **506** (2003) 250.

[64] ATLAS Collaboration, *Electron and photon energy calibration with the ATLAS detector using LHC Run 1 data*, Eur. Phys. J. C **74** (2014) 3071, arXiv: `1407.5063 [hep-ex]`.

[65] ATLAS Collaboration, *Electron and photon energy calibration with the ATLAS detector using 2015–2016 LHC proton-proton collision data*, JINST **14** (2019) P03017, arXiv: `1812.03848 [hep-ex]`.

[66] ATLAS Collaboration, *Measurement of the photon identification efficiencies with the ATLAS detector using LHC Run-1 data*, Eur. Phys. J. C **76** (2016) 666, arXiv: `1606.01813 [hep-ex]`.

[67] ATLAS Collaboration, *Photon identification in 2015 ATLAS data*, ATL-PHYS-PUB-2016-014, 2016, URL: `https://cds.cern.ch/record/2203125`.

[68] ATLAS Collaboration, *Topological cell clustering in the ATLAS calorimeters and its performance in LHC Run 1*, Eur. Phys. J. C **77** (2017) 490, arXiv: `1603.02934 [hep-ex]`.

[69] M. Cacciari, G. P. Salam, and G. Soyez, *The catchment area of jets*, JHEP **04** (2008) 005, arXiv: `0802.1188 [hep-ph]`.

[70] ATLAS Collaboration, *Performance of pile-up mitigation techniques for jets in pp collisions at $\sqrt{s} = 8$ TeV using the ATLAS detector*, Eur. Phys. J. C **76** (2016) 581, arXiv: `1510.03823 [hep-ex]`.

[71] ATLAS Collaboration, *Vertex Reconstruction Performance of the ATLAS Detector at $\sqrt{s} = 13$ TeV*, ATL-PHYS-PUB-2015-026, 2015, URL: `https://cds.cern.ch/record/2037717`.

[72] ATLAS Collaboration, *Measurement of the Higgs boson mass from the $H \to \gamma\gamma$ and $H \to ZZ^* \to 4\ell$ channels with the ATLAS detector*, Phys. Rev. D **90** (2014) 052004, arXiv: `1406.3827 [hep-ex]`.

[73] ATLAS Collaboration, *Electron efficiency measurements with the ATLAS detector using 2012 LHC proton-proton collision data*, Eur. Phys. J. C **77** (2017) 195, arXiv: `1612.01456 [hep-ex]`.

[74] ATLAS Collaboration, *Electron identification measurements in ATLAS using $\sqrt{s} = 13$ TeV data with 50 ns bunch spacing*, ATL-PHYS-PUB-2015-041, 2015, URL: `https://cds.cern.ch/record/2048202`.

[75] ATLAS Collaboration, *Measurements of fiducial and differential cross sections for Higgs boson production in the diphoton decay channel at $\sqrt{s} = 8$ TeV with ATLAS*, JHEP **09** (2014) 112, arXiv: `1407.4222 [hep-ex]`.

[76] ATLAS Collaboration, *Measurement of the muon reconstruction performance of the ATLAS detector using 2011 and 2012 LHC proton-proton collision data*, Eur. Phys. J. C **74** (2014) 3130, arXiv: `1407.3935 [hep-ex]`.

[77] ATLAS Collaboration, *Muon reconstruction performance of the ATLAS detector in proton–proton collision data at $\sqrt{s}$ =13 TeV*, Eur. Phys. J. C **76** (2016) 292, arXiv: `1603.05598 [hep-ex]`.

[78] M. Cacciari, G. P. Salam, and G. Soyez, *The anti-$k_t$ jet clustering algorithm*, JHEP **04** (2008) 063, arXiv: `0802.1189 [hep-ph]`.

[79] ATLAS Collaboration, *Tagging and suppression of pileup jets*, ATL-PHYS-PUB-2014-001, 2014, URL: `https://cds.cern.ch/record/1643929`.

[80] ATLAS Collaboration, *Jet energy scale measurements and their systematic uncertainties in proton-proton collisions at $\sqrt{s} = 13$ TeV with the ATLAS detector*, Phys. Rev. D **96** (2017) 072002, arXiv: `1703.09665 [hep-ex]`.

[81] ATLAS Collaboration, *Performance of b-jet identification in the ATLAS experiment*, JINST **11** (2016) P04008, arXiv: `1512.01094 [hep-ex]`.

[82] ATLAS Collaboration, *Optimisation of the ATLAS b-tagging performance for the 2016 LHC Run*, ATL-PHYS-PUB-2016-012, 2016, URL: `https://cds.cern.ch/record/2160731`.

[83] ATLAS Collaboration, *Evidence for the $H \to b\bar{b}$ decay with the ATLAS detector*, JHEP **12** (2017) 024, arXiv: `1708.03299 [hep-ex]`.

[84] ATLAS Collaboration, *Performance of missing transverse momentum reconstruction in proton-proton collisions at $\sqrt{s} = 7$ TeV with ATLAS*, Eur. Phys. J. C **72** (2012) 1844, arXiv: `1108.5602 [hep-ex]`.

[85] ATLAS Collaboration, *Performance of missing transverse momentum reconstruction with the ATLAS detector in the first proton–proton collisions at $\sqrt{s} = 13$ TeV*, ATL-PHYS-PUB-2015-027, 2015, URL: `https://cds.cern.ch/record/2037904`.

[86] ATLAS Collaboration, *Measurement of isolated-photon pair production in pp collisions at $\sqrt{s} = 7$ TeV with the ATLAS detector*, JHEP **01** (2013) 086, arXiv: `1211.1913 [hep-ex]`.

[87] ATLAS Collaboration, *Search for Scalar Diphoton Resonances in the Mass Range 65–600 GeV with the ATLAS Detector in pp Collision Data at $\sqrt{s} = 8$ TeV*, Phys. Rev. Lett. **113** (2014) 171801, arXiv: `1407.6583 [hep-ex]`.

[88] CDF Collaboration, T. Aaltonen et al., *Search for new particles decaying into dijets in proton-antiproton collisions at $\sqrt{s} = 1.96$ TeV*, Phys. Rev. D **79** (2009) 112002, arXiv: `0812.4036 [hep-ex]`.

[89] ATLAS Collaboration, *Measurement of Higgs boson production in the diphoton decay channel in pp collisions at center-of-mass energies of 7 and 8 TeV with the ATLAS detector*, Phys. Rev. D **90** (2014) 112015, arXiv: `1408.7084 [hep-ex]`.

[90] ATLAS Collaboration, *Luminosity determination in pp collisions at $\sqrt{s} = 8$ TeV using the ATLAS detector at the LHC*, Eur. Phys. J. C **76** (2016) 653, arXiv: `1608.03953 [hep-ex]`.

[91] G. Avoni et al., *The new LUCID-2 detector for luminosity measurement and monitoring in ATLAS*, JINST **13** (2018) P07017.

[92] ATLAS Collaboration, *Performance of the ATLAS Trigger System in 2010*, Eur. Phys. J. C **72** (2012) 1849, arXiv: `1110.1530 [hep-ex]`.

[93] ATLAS Collaboration, *Measurement of the photon identification efficiencies with the ATLAS detector using LHC Run 2 data collected in 2015 and 2016*, Eur. Phys. J. C **79** (2019) 205, arXiv: `1810.05087 [hep-ex]`.

[94] ATLAS Collaboration, *Expected performance of missing transverse momentum reconstruction for the ATLAS detector at $\sqrt{s} = 13$ TeV*, ATL-PHYS-PUB-2015-023, 2015, URL: `https://cds.cern.ch/record/2037700`.

[95] S. Dulat et al., *New parton distribution functions from a global analysis of quantum chromodynamics*, Phys. Rev. D **93** (2016) 033006, arXiv: `1506.07443 [hep-ph]`.

[96] L. A. Harland-Lang, A. D. Martin, P. Motylinski, and R. S. Thorne, *Parton distributions in the LHC era: MMHT 2014 PDFs*, Eur. Phys. J. C **75** (2015) 204, arXiv: `1412.3989 [hep-ph]`.

[97] ATLAS and CMS Collaborations, *Combined Measurement of the Higgs Boson Mass in pp Collisions at $\sqrt{s} = 7$ and 8 TeV with the ATLAS and CMS Experiments*, Phys. Rev. Lett. **114** (2015) 191803, arXiv: `1503.07589 [hep-ex]`.

[98] A. L. Read, *Presentation of search results: The $CL_s$ technique*, J. Phys. G **28** (2002) 2693.

[99] G. Cowan, K. Cranmer, E. Gross, and O. Vitells, *Asymptotic formulae for likelihood-based tests of new physics*, Eur. Phys. J. C **71** (2011) 1554, arXiv: `1007.1727 [physics.data-an]`, Erratum: Eur. Phys. J. C **73** (2013) 2501.